

A SIMULATION TOOL SUITE FOR THE MODELING AND  
OPTIMIZATION OF MULTIPLE QUANTUM  
WELL STRUCTURES

by

JEFFERY WAYNE ALLEN

Presented to the Faculty of the Graduate School of  
The University of Texas at Arlington in Partial Fulfillment  
of the Requirements  
for the Degree of

MASTER OF SCIENCE IN ELECTRICAL ENGINEERING

THE UNIVERSITY OF TEXAS AT ARLINGTON

December 2005

## ACKNOWLEDGEMENTS

I would like to express my sincere gratitude to my advisor, Dr. Kambiz Alavi, for his guidance, constant encouragement and support during the period of my research. Working with Dr. Alavi, has provided me with a great opportunity to learn and grow both as a student and a person, for which I am very grateful. I would also like to thank my graduate committee members, Dr. J. Bredow and Dr. W. Zhou for their valuable comments and suggestions.

This thesis is dedicated to my wife, Monica and my parents Gary and Donna Allen. Without their constant love and support, this work never would have been possible. Working full time and going to school has been a family struggle and I will be indebted to them for sticking with me to help me realize my dreams. I would also like to thank my brothers; Chris and Wade, for their encouragement and support that has helped me persevere and excel in all my endeavors.

Special thanks go out to all my friends who have helped me through all the good and bad times, there are too many to name but you know who you are.

November 11, 2005

## ABSTRACT

### A SIMULATION TOOL SUITE FOR THE MODELING AND OPTIMIZATION OF MULTIPLE QUANTUM WELL STRUCTURES

Publication No. \_\_\_\_\_

Jeffery Wayne Allen, M.S.

The University of Texas at Arlington, 2005

Supervising Professor: Kambiz Alavi

This thesis aims to develop a suite of computational tools for design, analysis, and simulation of semiconductor multiple quantum well structures with a user-friendly GUI. The research project focuses on the electrical and optical aspects of user defined quantum well structures, and allows the user to vary design parameters to optimize the structure for different device applications and functionality. Specifically the thesis delves into the design and analysis of different quantum well structures as they relate to band gap engineering. Key features of this computational suite include relationship to electrical field, doping profiles and optical transitions.

The quantum well structures presented are single, double, stepped, and chirped quantum wells, with uniform, modulated, or planar doping. The computational suite can be applied to the calculation of energy levels and band bending in intraband and interband optical transitions in quantum well infrared photodetectors (QWIPs) and quantum well electroabsorption and electroreflection modulators.

## TABLE OF CONTENTS

ACKNOWLEDGEMENTS.....	ii
ABSTRACT .....	iii
LIST OF ILLUSTRATIONS.....	viii
LIST OF TABLES.....	xi
Chapter	
1. INTRODUCTION.....	1
1.1 Optimization of Materials.....	2
1.2 Thesis Outline.....	3
2. BACKGROUND THEORY .....	6
2.1 Physical Interpretation of the Wavefunction .....	7
2.2 Infinite Quantum Well .....	8
2.3 Finite Rectangular Quantum Well .....	11
2.3.1 Exact Solution.....	11
2.3.2 Numerical Analysis .....	16
2.4 Runge-Kutta Method .....	17
2.4.1 Adaptive Step Size.....	19
2.4.2 Selection of Step Size .....	23
2.4.3 Continuous Interpolation Polynomials .....	24

2.5 Shooting Methods .....	26
2.5.1 Simple Shooting Method .....	26
2.5.2 Shooting to a Fitting Point.....	28
2.6 Simple Model: Undoped Case. ....	33
2.7 Self Consistent Model: Doped Case. ....	35
2.7.1 Poisson Equation .....	35
2.7.2 Self Consistent Schrödinger Poisson Equation.....	41
3. QUANTUM-WELL USER ENTERED SIMULATION TOOL (QUEST)...	45
3.1 Developing the Suite of Tools .....	45
3.2 QUEST Features.....	46
3.2.1 Input Features.....	46
3.2.2 Error Handling.....	50
3.2.3 Running the Program.....	51
3.2.4 Flow Chart of QUEST Hierarchy.....	56
3.3 Example of a Complete QUEST Run.....	64
4. SIMULATION RESULTS.....	72
4.1 Undoped Rectangular Well.....	72
4.2 Doped Rectangular Well.....	74
4.3 Effects of Electric Field .....	76
4.3.1 Rectangular Well with Applied Electric Field.....	77
4.4 Asymmetric Well structures: Stepped Well Structures .....	79
4.5 Triple Well Structures.....	81

4.6 Chirped Well Structure.....	83
5. DEVICE APPLICATION.....	87
5.1 Quantum Well Infrared Photodetector.....	87
5.2 Application of Electric Field.....	88
5.3 Calculation of Absorption.....	88
5.3.1 Calculation of Absorption Spectrum.....	89
5.4 Simulated Structure Parameters.....	89
6. SUMMARY AND FUTURE WORK.....	94
6.1 Specific Achievements.....	94
6.2 Future Work.....	95
REFERENCES .....	96
BIOGRAPHICAL INFORMATION.....	101

## LIST OF ILLUSTRATIONS

Figure	Page
2.1 Potential energy of an infinite well, with width $L_x$ . Also indicated are the lowest five energy levels in the well. ....	9
2.2 (a) Energy levels, wavefunctions and (b) Probability density functions of an infinite quantum well .....	11
2.3 Finite quantum well.....	11
2.4 Graph of $k_2 \sqrt{\frac{m_b}{m_w}} \frac{L_w}{2}$ against $k_1 \frac{L_w}{2}$ and $\sqrt{\frac{2m_w V_0}{\hbar^2}} \frac{L_w}{2}$ . The solutions of the finite rectangular quantum well.....	15
2.5 The wavefunctions for the solutions found in figure 2.4 .....	16
2.6 Graph illustrating the Midpoint method.....	18
2.7 Step doubling as a means for adaptive step size control in fourth order Runge-Kutta.....	20
2.8 Method of shooting from an initial point $x=a$ to $x=b$ .....	27
2.9 Shooting to an intermediate fitting point, $x_f$ .....	28
2.10 Modulation doped single quantum well.....	35
2.11 Electric field strength from an infinite plane of charge from a volume density of dopants, $d(x)$ and thickness, $\delta x$ .....	36
2.12 Areal charge density for a 100 angstrom GaAs well, n-type doped to $1 \times 10^{18} \text{ cm}^{-3}$ surrounded by undoped $\text{Ga}_{0.8}\text{Al}_{0.2}\text{As}$ barriers .....	39



2.13	The electric field strength due to the charge distribution shown in figure 2.12.....	40
2.14	The potential due to the donor (electron) charge distribution.....	41
2.15	Block diagram of the iterative process used to solve the self consistent model.....	43
2.16	The sum of the band edge potential, $V_{CB}$ , Poisson's potential, $V_{\rho}$ , for the single quantum well of Figure 12.....	44
3.1	User Interface for QUEST at start-up.....	47
3.2	Error message displayed for incorrect input data.....	50
3.3	Progress bar while program is busy.....	51
3.4	Dialog box to proceed to next structure or go to next step.....	52
3.5	Dialog box to proceed to the Poisson self-consistent model.....	52
3.6	User defined variables for the Poisson self-consistent model.....	53
3.7	'Browse for folder' selection box.....	55
3.8	Flow chart representing the QUEST hierarchy.....	57
3.9	Input screen for Example 1- first well structure.....	65
3.10	Output screen 1- Example 1 solutions (energy levels and wavefunctions).....	66
3.11	User chooses to simulate another well by clicking 'YES'.....	67
3.12	Input screen for Example 2- Second well structure.....	67
3.13	Output screen 2- Example 2 solutions (energy levels and wavefunctions).....	68
3.14	User chooses to continue with the Self consistent model by clicking 'YES'.....	69
3.15	Input screen for Example 2- doping structure.....	69

3.16	User chooses the well for further calculations (here Example 2) .....	70
3.17	Output Screen 3- Self consistent solutions for Example 2 (Energy levels and Wave functions) .....	71
4.1	Schematic of the tilting of conduction and valence band under the influence of and electric field .....	76

## LIST OF TABLES

Table	Page
2.1 Classical variables and the corresponding quantum operator .....	8
2.2 RK5(4)7FM embedded pair (DOPRI5) .....	25
4.1 The wave functions and the solutions of a finite rectangular quantum well where the Barrier width = 150 Å, $L_w = 100$ Å, $m_w = 0.067$ , $m_b = 0.0919$ , $V_0 = 0.302$ eV .....	73
4.2 Solutions of a finite rectangular quantum well where the Barrier width = 150 Å, $L_w = 100$ Å, $m_w = 0.067$ , $m_b = 0.0919$ , $V_0 = 0.302$ eV .....	74
4.3 The wave functions and the solutions of a finite rectangular quantum well where the Barrier width = 50 Å, $L_w = 100$ Å, $m_w = 0.067$ , $m_b = 0.0919$ , $V_0 = 0.251$ eV with modulation doping within 10 Å at both ends of the profile $-100 \text{ Å} \leq x \leq -90 \text{ Å}$ and $90 \text{ Å} \leq x \leq 100 \text{ Å}$ , $N_D = 4E18 \text{ cm}^{-3}$ .....	75
4.4 Solutions of a finite rectangular quantum well where the Barrier width = 50 Å, $L_w = 100$ Å, $m_w = 0.067$ , $m_b = 0.0919$ , $V_0 = 0.251$ eV with modulation doping within 10 Å at both ends of the profile $-100 \text{ Å} \leq x \leq -90 \text{ Å}$ and $90 \text{ Å} \leq x \leq 100 \text{ Å}$ , $N_D = 4E18 \text{ cm}^{-3}$ .....	76
4.5 The wave functions and the solutions of a finite rectangular quantum well where the Barrier width = 200 Å, $L_w = 100$ Å, $m_w = 0.0665$ , $m_b = 0.0957$ , $V_0 = 0.262$ eV, Applied electric field $E = 50$ kV/cm .....	78
4.6 Solutions of a finite rectangular quantum well where the Barrier width = 200 Å, $L_w = 100$ Å, $m_w = 0.0665$ , $m_b = 0.0957$ , $V_0 = 0.262$ eV, Applied electric field $E = 50$ kV/cm .....	79

4.7	The wave functions and the solutions of a finite rectangular quantum well where the $\text{Al}_{0.44}\text{Ga}_{0.56}\text{As}$ barrier of width = 280 Å, well width of $L_w = 60$ Å with a step of $\text{Al}_{0.18}\text{Ga}_{0.82}\text{As}$ of width 90 Å, and well mass of $m_w=0.0665$ , barrier mass of $m_b=0.1$ , step mass of $m_s=0.08$ and barrier height of $V_0=0.33$ eV, step height $V_s=0.15$ eV .....	80
4.8	Solutions of a finite rectangular quantum well where the $\text{Al}_{0.44}\text{Ga}_{0.56}\text{As}$ barrier of width = 280 Å, well width of $L_w = 60$ Å with a step of $\text{Al}_{0.18}\text{Ga}_{0.82}\text{As}$ of width 90 Å, and well mass of $m_w=0.0665$ , barrier mass of $m_b=0.1$ , step mass of $m_s=0.08$ and barrier height of $V_0=0.33$ eV, step height $V_s=0.15$ eV .....	81
4.9	The wave functions and the solutions of a quantum well structure with three $\text{Ga}_{0.47}\text{In}_{0.53}\text{As}$ quantum wells with well width of $L_w = 64$ Å, 42 Å and 28 Å respectively separated by $\text{Al}_{0.48}\text{In}_{0.52}\text{As}$ barrier of width = 16 Å, and well mass of $m_w = 0.04$ , barrier mass of $m_b=0.075$ and barrier height of $V_0=0.53$ eV .....	82
4.10	Solutions of a quantum well structure with three $\text{Ga}_{0.47}\text{In}_{0.53}\text{As}$ quantum wells with well width of $L_w = 64$ Å, 42 Å and 28 Å respectively, separated by $\text{Al}_{0.48}\text{In}_{0.52}\text{As}$ barrier of width = 16 Å, and well mass of $m_w = 0.04$ , barrier mass of $m_b=0.075$ and barrier height of $V_0=0.53$ eV .....	83
4.11	The wave functions and the solutions of a chirped rectangular quantum well where the Barrier width = 150 Å, $L_w \sim 100$ Å (36 monolayers), $m_w = 0.067$ , $m_b = 0.15$ , $V_0=0.044$ eV .....	84
4.12	The wave functions and the solutions of a chirped rectangular quantum well where the Barrier width = 150 Å, $L_w \sim 100$ Å (36 monolayers), $m_w = 0.067$ , $m_b = 0.15$ , $V_0 = 0.044$ eV, Applied electric field $E = 128.571$ kV/cm .....	85
4.13	The wave functions and the solutions of a chirped rectangular quantum well where the Barrier width = 150 Å, $L_w \sim 100$ Å (36 monolayers), $m_w = 0.067$ , $m_b = 0.15$ , $V_0=0.044$ eV, Applied electric field $E=257.143$ kV/cm .....	86
4.14	Solutions of a quantum well structure where the Barrier width = 150 Å, $L_w \sim 100$ Å (36 monolayers), $m_w=0.067$ , $m_b=0.15$ , $V_0=0.044$ eV .....	86

5.1 Plots that show the wavefunctions, states and absorption spectra for the well structure with  $\text{In}_{0.65}\text{Ga}_{0.35}\text{As}$  wells of  $50\text{\AA}$  and  $100\text{\AA}$ ,  $\text{In}_{0.52}\text{Al}_{0.48}\text{As}$  center barrier of  $30\text{\AA}$ , surrounding barrier widths of  $150\text{\AA}$  under applied electric field of 0, -50 and 50 kV/cm. The effective mass values of the  $\text{In}_{0.52}\text{Al}_{0.48}\text{As}$  barrier and the  $\text{In}_{0.65}\text{Ga}_{0.35}\text{As}$  are  $0.13663 m_0$  and  $0.03654 m_0$  ..... 92

## CHAPTER 1

### INTRODUCTION

A quantum well is defined as a potential well that confines particles in one dimension, and forces them to occupy a planar region. The effects of quantum confinement become pronounced as the quantum well thickness approaches the de Broglie wavelength of the particles namely electrons and holes. This leads to energy levels that are different from those observed in larger sized semiconductor structures fabricated from comparable materials. This phenomenon dictates that the carriers can have only discrete energy values called energy subbands.

Quantum wells are fabricated by sandwiching narrower bandgap material such as Gallium Arsenide (GaAs) between two layers of a wider bandgap material such as Aluminium arsenide (AlAs). Electrons in quantum wells have a sharper density of states than bulk materials and can be used for optical applications such diode lasers, spatial light modulators (SLMs), and quantum well infrared photodetectors (QWIPs) as well as semiconductor electronic devices such as high electron mobility transistors (HEMTs).

Although devices based on quantum wells are used widely in several applications like optical communication systems, many of the operating characteristics are not fully understood. This thesis focuses on studying the physics behind III-V materials and devices and using the accumulated knowledge and experimental data to

develop an integrated suite of simulation tools that can be used for the preliminary characterization of a device based on its material properties.

### 1.1 Optimization of Materials

As described in the previous section, a quantum well is fabricated by depositing a smaller bandgap material between two layers of barrier (larger bandgap) material. In a semiconductor heterostructure, this forms a potential well which is observed in both the valence and conduction bands [4, 5]. The well is capable of capturing carriers namely electrons and holes which gives rise to quantum confinement leading to dramatic changes in optical and transport properties of the carriers.

Growth of viable devices that serve the application for which they are fabricated is contingent on the development of reliable and predictable heterostructures. It is essential to accurately simulate structural, optical and electronic transport characteristics which affect device function so that a particular growth methodology or process can be chosen for fabrication to produce the desired results [6]. These operational characteristics are governed by the composition, thickness, doping and placement of dopants in the quantum well and surrounding barriers [7]. Material composition and profiles of the well and barriers determine the potential depth, effective masses and internal strains. These attributes affect the wavefunctions and quantum confined energies which in turn determine the density of states for optical absorption and emission as well as the electron occupancy ratios and scattering cross section area.

It is of great interest to have a simulation tool which allows a user to design and analyze quantum wells of arbitrary shapes and composition. Such a tool maybe used to

determine the operating characteristics of a device fabricated based on the simulated quantum well. The primary goal of this thesis is to develop a user-friendly quantum well simulation tool suite to perform the following functions:

- (a) Calculate Eigen energies/states and wavefunctions for arbitrary well structures
- (b) Determine the effects of electric field and doping profiles on well characteristics
- (c) Calculate absorption coefficients for the user defined quantum well
- (d) Comparison of simulated characteristics to experimental results

To summarize, the simulation tool aims to aid in semiconductor epitaxial methods such as molecular beam epitaxy, primarily in the design and building of material structures that take advantage of the quantum mechanical effects using bandgap engineering. Additionally the simulation tool may also be applied to research efforts that examine the outcome of changing size, shape and material composition of wells and consequently how these affect various electronic properties of the material. Furthermore, device characteristics can be modified using an external electric field. Such effects have also been simulated as part of this thesis and are presented in a later section.

## 1.2 Thesis Outline

This thesis is organized in the following manner.

Chapter 1 gives a general introduction to the thesis and the aims that motivate this work. A short thesis is provided that gives a brief summary of the topics covered in each chapter.



Chapter 2 starts with basic quantum mechanics theory underlying this research. It begins with an explanation of the physical interpretation of a wavefunction. Next the Schrödinger's equation is solved for the case of the infinite quantum well. Boundary conditions are refined to develop the case of the finite rectangular quantum well. Both the exact and numerical solution for a single bounded well are discussed. The Runge-Kutta and Shooting method that are used to solve the differential equations is described in detail. The general quantum theory is then particularized to address the simple rectangular well in both the undoped and doped case (Self consistent Poisson equation).

Chapter 3 is designed to be a user manual for the Quantum-Well User Entered Simulation Tool (QUEST) that is developed in this research. Apart from the user instructions to run the program, installation requirements and software implementation are also detailed. An example run of the software is presented to guide the user through the program.

Chapter 4 outlines simulation results for well structures and QUEST results for these varied structures are compared to previously published data. The structures that are presented include an Undoped Rectangular Well, Doped Rectangular Well, Asymmetric Well structures, Triple Well Structures and Chirped Well Structure. Effects of external applied electric field are also discussed with relevant examples and simulations.

Chapter 5 demonstrates the application of the developed simulation tool suite to a device simulation. A Quantum Well Infrared Photodetector (QWIP) is used to bring forth the functionality of QUEST as an effective pre-fabrication procedure for bandgap

engineering. A QWIP was chosen because of the interest of the Optoelectronic Research Group at UTA in the design, development and fabrication of such devices.

Chapter 6 summarizes the specific achievements of this research work and provides suggestions for future development and directions for this research.

## CHAPTER 2

### BACKGROUND THEORY

The infinite quantum well is the simplest confinement potential to study and is the foundation of this research. The theory underlying the infinite quantum well develops the standard assumptions and their consequences for a one-dimensional confinement potential.

The general solution to the Schrödinger Equation starts from the classical description of the total energy,  $E$ , which is equal to the sum of the kinetic energy,  $T$ , and the potential energy,  $V$

$$E = T + V = \frac{p^2}{2m} + V(x) \quad (1)$$

A wavefunction,  $\Psi$ , is defined to convert the energy equation into a wave equation (Equation 2) [8]. This is achieved by multiplying each term in the energy equation by the defined wavefunction,  $\Psi$

$$E\Psi = \frac{p^2}{2m}\Psi + V(x)\Psi \quad (2)$$

To incorporate the de Broglie wavelength of the particle, we introduce the operator  $-\frac{\hbar^2 \partial^2}{\partial x^2}$ , which provides the square of the momentum,  $p$ . When applied to a plane wave we obtain Equation 3 [8, 9]

$$-\hbar^2 \frac{\partial^2 \Psi}{\partial x^2} = \hbar^2 k^2 \Psi = p^2 \Psi \text{ for } \Psi = e^{i(kx - \omega t)} \quad (3)$$

where  $k$  is the wavenumber ( $k = 2\pi / \lambda$ ). Replacing the momentum squared,  $p^2$ , in equation (2) by this operator yields the one-dimensional time-independent Schrödinger equation (Equation 4).

$$-\frac{\hbar}{2m} \frac{d^2 \Psi(x)}{dx^2} + V(x)\Psi(x) = E\Psi(x) \quad (4)$$

### 2.1 Physical Interpretation of the Wavefunction

The particle-wave duality principle is applied to the Schrödinger equation to explain the use of a wavefunction to describe a confined particle. While this helps simplify the mathematical solution, it does not provide adequate insight into the physical meaning of the wavefunction.

Quantum theory postulates that the probability density function,  $P(x)$ , associated with a particle is proportional to the product of the wavefunction of the particle,  $\Psi(x)$ , and its complex conjugate,  $\Psi^*(x)$ .

$$P(x) = \Psi(x)\Psi^*(x) \quad (5)$$

The probability density function,  $P(x)$ , integrated over a specific volume provides the probability that the particle described by the wavefunction is within that volume. The probability function is normalized to indicate that the probability of finding a particle in a given volume equals 100%. The magnitude of the wavefunction is calculated with this normalization (Equation 6) [8, 10]

$$\int_{-\infty}^{\infty} P(x)dx = 1 \quad (6)$$

The probability density function is used to find the properties of the particle using quantum operators. The expected value of the probability density function for a particle,  $f(x,p)$ , is described by the wavefunction and is given by

$$\langle f(x, p) \rangle = \int_{-\infty}^{\infty} \Psi(x) F(x) \Psi^* dx \quad (7)$$

where  $F(x)$  is the quantum operator associated with the function. A list of quantum operators corresponding to classical variables is provided in Table 2.1 [8].

Table 2.1 Classical variables and the corresponding quantum operator [8]

	Classical Variable	Quantum Operator
Position	$x$	$x$
A function which depends only on position	$f(x)$	$F(x)$
Momentum	$p$	$\frac{\hbar}{i} \frac{\partial}{\partial x}$
Energy	$E$	$-\frac{\hbar}{i} \frac{\partial}{\partial t}$

## 2.2 Infinite Quantum Well

The one-dimensional infinite quantum well is used to illustrate specific properties of quantum mechanical systems. In an infinite well, the potential is zero within the well ( $x = 0$  and  $x = Lx$ ) and infinite outside the well. Figure 2.1 shows the potential of a well and the first five energy levels an electron can occupy.

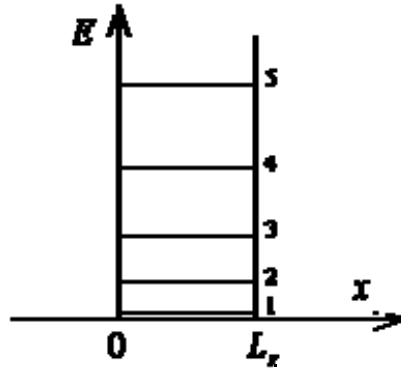


Figure 2.1 Potential energy of an infinite well, with width  $L_x$ . Also indicated are the lowest five energy levels in the well.[8]

The energy levels in an infinite quantum well are calculated by solving Schrödinger's equation (Equation 4) with the potential,  $V(x)$ . Inside the well the potential,  $V(x) = 0$  and Schrödinger's equation reduces to the following form.

$$-\frac{\hbar^2}{2m} \frac{d^2\Psi(x)}{dx^2} = E\Psi \quad \text{for } 0 < x < L_x \quad (8)$$

The general solution to this differential equation is

$$\Psi(x) = A \sin\left(\frac{\sqrt{2mE}}{\hbar}x\right) + B \cos\left(\frac{\sqrt{2mE}}{\hbar}x\right) \quad \text{for } 0 < x < L_x \quad (9)$$

where the coefficients  $A$  and  $B$  are determined by applying boundary conditions. Since the potential is infinite on both sides of the well, the probability of finding an electron outside the well and at the well boundary is zero. Therefore the wave function must be zero on both sides of the infinite quantum well [8, 11].

$$\Psi(0) = 0 \quad \text{and} \quad \Psi(L_x) = 0 \quad (10)$$

These boundary conditions imply that the coefficient  $B$  must be zero and the argument of the sine function must equal to a multiple of  $\pi$  at the edge of the quantum well

$$\frac{\sqrt{2mE_n}}{\hbar} L_x = n\pi, \text{ with } n = 1, 2, \dots \quad (11)$$

where  $n$  represents quantized energy levels. The resulting values of the energy,  $E_n$ , are

$$E_n = \frac{\hbar^2}{2m^*} \left(\frac{n}{2L_x}\right)^2, \text{ with } n = 1, 2, \dots \quad (12)$$

The corresponding normalized wave functions,  $\Psi_n(x)$ , are

$$\Psi_n(x) = \sqrt{\frac{2}{L_x}} \sin\left(\frac{\sqrt{2mE_n}}{\hbar} x\right) \text{ for } 0 < x < L_x \quad (13)$$

The coefficient  $A$  is determined by setting the probability of finding the electron in the well to unity. [4, 8]

$$\int_0^{L_x} \Psi_n(x) \Psi_n^*(x) dx = 1 \quad (14)$$

The lowest possible energy,  $E_1$ , is not zero although the potential within the well is zero. The discrete energy values are obtained by solving for the Eigen values of the Schrödinger equation [11]. The energy difference between adjacent energy levels increases as the energy increases. The wavefunctions corresponding to each energy level are shown in Figure 2.2(a). Each wavefunction is shifted by the corresponding energy and scaled. The probability density functions for the first five energy levels are shown in Figure 2.2(b).

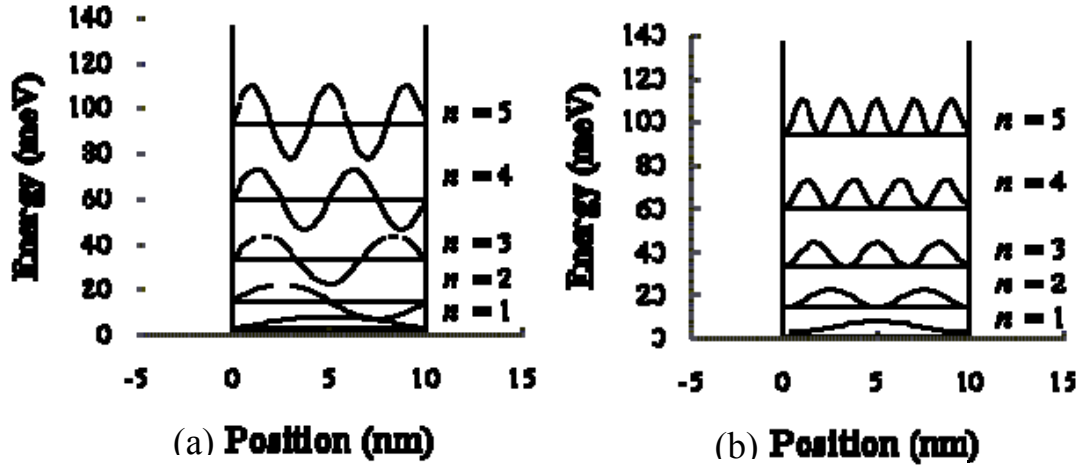


Figure 2.2 (a) Energy levels, wavefunctions and (b) Probability density functions of an infinite quantum well [8]

### 2.3 Finite Rectangular Quantum Well

The finite rectangular quantum well is characterized by a zero potential inside the well and a potential  $V_0$  outside the well. The origin is chosen in the middle of the well.

#### 2.3.1 Exact Solution

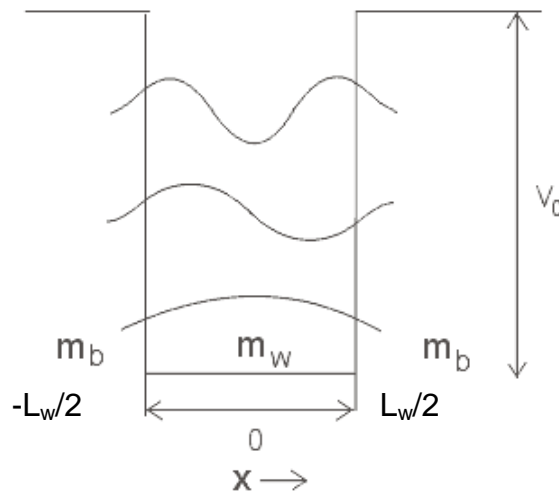


Figure 2.3 Finite quantum well [12]



A simple model of the energy levels in a finite quantum well is solved below using an analytic solution. The Schrödinger equation is solved for a finite potential to give the values of various energy levels within the well. Consider a potential well of width,  $L_w$  and barrier height,  $V_0$ , centered around the origin [9]. The Schrödinger equation can be rewritten using the condition that potential inside the well is zero and outside the well is  $V_0$ .

$$V_0 = \begin{cases} 0, & |x| < L_w/2 \\ V_0, & |x| \geq L_w/2 \end{cases} \quad (15)$$

Inside the well

$$\frac{\hbar^2}{2m} \frac{d^2\Psi(x)}{dx^2} + k_1\Psi(x) = 0 \quad |x| < L_w/2 \quad \text{with} \quad k_1 = \sqrt{\frac{2mE}{\hbar^2}} \quad (16)$$

Outside the well/in the barrier region

$$\frac{\hbar^2}{2m} \frac{d^2\Psi(x)}{dx^2} - k_2\Psi(x) = 0 \quad |x| > L_w/2 \quad \text{with} \quad k_2 = \sqrt{\frac{2m(V_0 - E)}{\hbar^2}} \quad (17)$$

For even wavefunctions, the solution of the Schrödinger equation within the well is given by

$$\Psi(x) = \begin{cases} C_1 \exp(-k_2|x| - L_w) & |x| > L_w/2 \\ C_2 \cos k_1 x & |x| < L_w/2 \end{cases} \quad (18)$$

Using the boundary conditions in which the wave function and its first derivative divided by the effective mass  $(1/m)(d\Psi/dx)$  are continuous at the interface between the barrier and the well [11].

$$\Psi\left(\frac{L_w^+}{2}\right) = \Psi\left(\frac{L_w^-}{2}\right) \text{ and } \frac{1}{m_b} \frac{d}{dx} \Psi\left(\frac{L_w^+}{2}\right) = \frac{1}{m_w} \frac{d}{dx} \Psi\left(\frac{L_w^-}{2}\right) \quad (19)$$

we obtain

$$C_1 = C_2 \cos(k_1 \frac{L_w}{2}) \quad (20)$$

$$\frac{k_2}{m_b} C_1 = \frac{k_1}{m_w} C_2 \sin(k_1 \frac{L_w}{2}) \quad (21)$$

Eliminating  $C_1$  and  $C_2$ , we obtain the Eigen equation or the quantization condition:

$$k_2 = \frac{m_b k_1}{m_w} \tan(k_1 \frac{L_w}{2}) \quad (22)$$

The Eigen energy can be found from the above equation by substituting  $k_l$  and  $k_2$  [10].

Similarly for odd wave functions, we have of the form

$$\Psi(x) = \begin{cases} C_1 \exp\left[-k_2\left(x - \frac{L_w}{2}\right)\right] & x > L_w/2 \\ C_2 \sin(k_1 x) & |x| \leq L_w/2 \\ -C_1 \exp\left[k_2\left(x - \frac{L_w}{2}\right)\right] & x < -L_w/2 \end{cases} \quad (23)$$

The boundary conditions give

$$C_1 = C_2 \sin(k_1 \frac{L_w}{2}) \quad (24)$$

$$\frac{-k_2 C_1}{m_b} = \frac{k_1}{m_w} C_2 \cos(k_1 \frac{L_w}{2}) \quad (25)$$

The Eigen equation is thus given by

$$k_2 = -\frac{m_b k_1}{m_w} \cot(k_1 \frac{L_w}{2}) \quad (26)$$

which determines the Eigen energy, E, for the odd wave function using  $k_1$  and  $k_2$ . In general, the solutions for the quantized Eigen energies can be obtained by finding  $k_1L_w/2$  and  $k_2L_w/2$  directly from a graphical approach since

$$\left(k_1 \frac{L_w}{2}\right)^2 + \frac{m_w}{m_b} \left(k_2 \frac{L_w}{2}\right)^2 = \frac{2m_w V_0}{\hbar^2} \left(\frac{L_w}{2}\right)^2 \quad (27)$$

and

$$k_2 \sqrt{\frac{m_b}{m_w}} \frac{L_w}{2} = \frac{m_b k_1}{m_w} \frac{L_w}{2} \tan\left(k_1 \frac{L_w}{2}\right) \quad \text{for even solutions} \quad (28)$$

$$k_2 \sqrt{\frac{m_b}{m_w}} \frac{L_w}{2} = -\frac{m_b k_1}{m_w} \frac{L_w}{2} \cot\left(k_1 \frac{L_w}{2}\right) \quad \text{for odd solutions} \quad (29)$$

In the case where the mass of the particle in the barrier differs from the mass of the particle in the well, we introduce a scaling factor to account for this [9]. Plotting

$k_2 \sqrt{\frac{m_b}{m_w}} \frac{L_w}{2}$  against  $k_1 \frac{L_w}{2}$  produces the graphs below, the potential generates a circle of

radius  $\sqrt{\frac{2m_w V_0}{\hbar^2}} \frac{L_w}{2}$ . The energy levels in the well are found from the intersection of the

tangent and cotangent relationships with the circle within the positive quarter. Figures

2.4 and 2.5 further demonstrate the use of this technique to solve a finite rectangular

quantum well [9]. The simulation was carried out by a program written in Matlab for a

finite rectangular quantum well where Barrier width = 150 Å,  $L_w = 100$  Å,  $m_w = 0.067$ ,

$m_b = 0.0919$ ,  $V_0 = 0.302$  eV

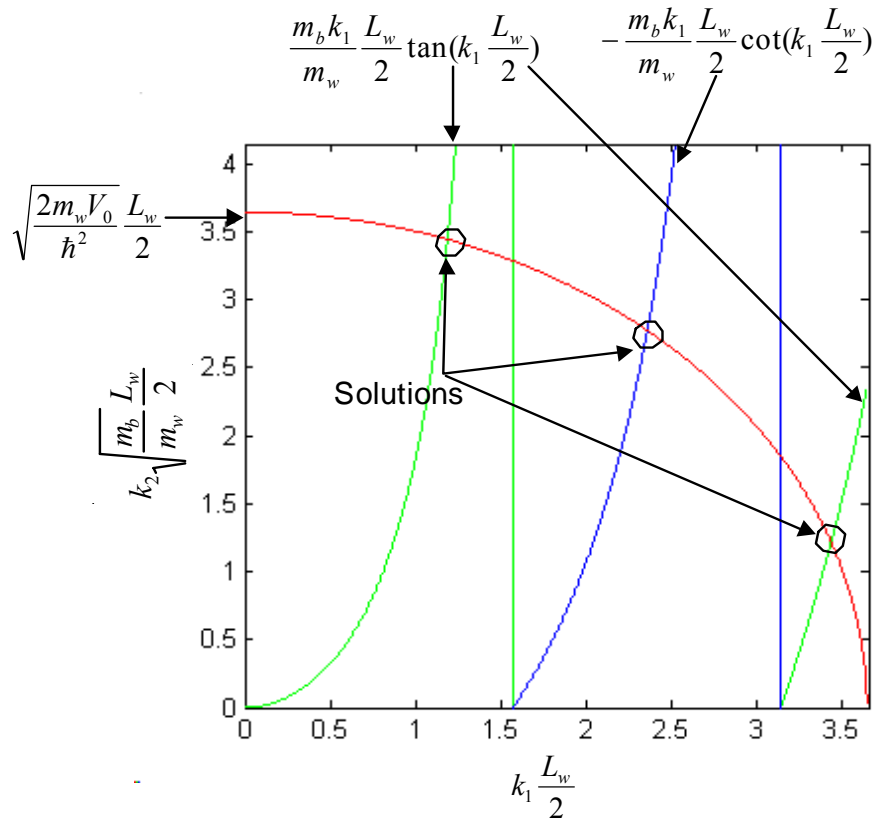


Figure 2.4 Graph of  $k_2 \sqrt{\frac{m_b}{m_w}} \frac{L_w}{2}$  against  $k_1 \frac{L_w}{2}$  and  $\sqrt{\frac{2m_w V_0}{\hbar^2}} \frac{L_w}{2}$ . The solutions of the finite rectangular quantum well where the Barrier width =  $150 \text{ \AA}$ ,  $L_w = 100 \text{ \AA}$ ,  $m_w = 0.067$ ,  $m_b = 0.0919$ ,  $V_0 = 0.302 \text{ eV}$  are shown by the circles.

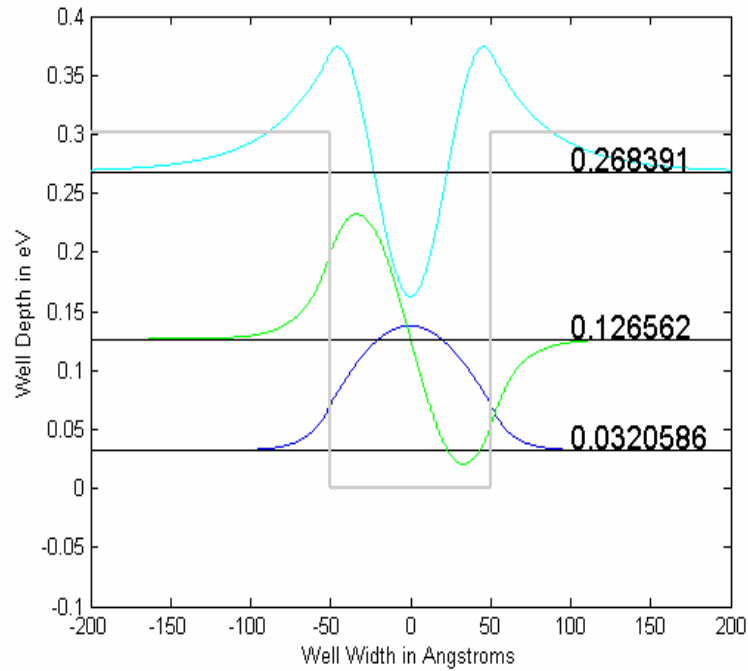


Figure 2.5 The wavefunctions for the solutions found in figure 2.4

### 2.3.2 Numerical Analysis

A differential equation describes the relation between an unknown function and its derivatives. The solution of a differential equation is usually in the form of a function that satisfies the relation stated in the problem (the differential equation itself) along with some additional condition (like boundary or initial conditions) [13]. In a canonical initial value problem, the behavior of the system is described by an ordinary differential equation (ODE) of the form  $dx/dt = f(x,t)$  where  $f$  is a known function,  $x$  is the state of the system, and  $dx/dt$  is the time derivative of  $x$ . Typically,  $x$  and  $dx/dt$  are vectors. As the name suggests, in an initial value problem  $x$  at time=0 is known and we wish to follow  $x$  over time thereafter [13].

The standard differential equation solver is the fourth-order Runge-Kutta method. It has more precision than the Euler's algorithm from which it is derived and offers several attractive features such as ease of programming and mathematical simplicity. With the addition of an adaptive or self-adjusting step size, the fourth-order Runge-Kutta method is both robust and capable of providing solutions to complex problems. In the next section a basic derivation of the Runge-Kutta method is provided in addition to background theory and underlying equations [14].

#### 2.4 Runge-Kutta Method

The approximate solution for a given point in space using the Euler method is  $y_{n+1} = y_n + hf(x_n, y_n)$  which advances a solution from  $x_n$  to  $x_{n+1} \equiv x_n + h$ . It advances the solution through an interval  $h$ , and uses the derivative at the beginning of that interval to avoid discontinuities at the boundaries. This implies that the error in a single step is limited to only one power of  $h$  smaller than the correction [15].

Euler's method is not very accurate, when compared to more complicated methods using an equivalent step size and can also be unstable. Thus a more complex method, namely the Runge-Kutta solver, is adopted for this development. The Runge-Kutta solver uses the following method to find the solutions to a given system of differential equations. A trial step to the midpoint of the interval is taken. Then the values of both  $x$  and  $y$  at that midpoint are used to compute the “real” step across the whole interval [15]. This is illustrated below in Figure 2.6.

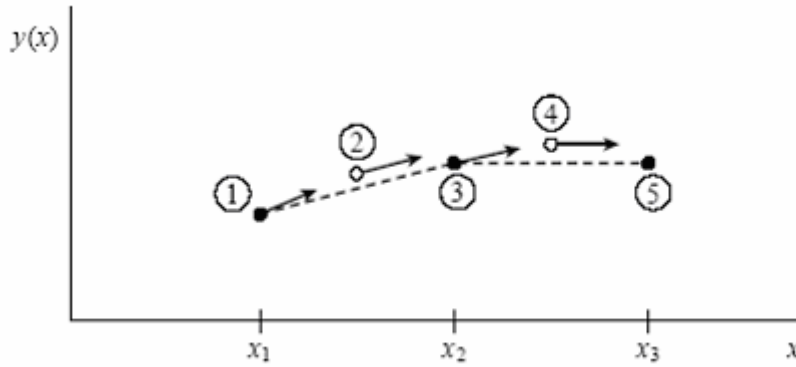


Figure 2.6 Graph illustrating the Midpoint method. Second order accuracy is obtained by using the initial derivative at each step to find a point halfway across the interval, then using the midpoint derivative across the full width of the interval. In the figure, filled dots represent final function values, while open dots represent function values that are discarded once their derivatives have been calculated and used.[15]

Putting this idea in the form of equations,

$$\begin{aligned}
 k_1 &= hf(x_n, y_n) \\
 k_2 &= hf\left(x_n + \frac{1}{2}h, y_n + \frac{1}{2}k_1\right) \\
 y_{n+1} &= y_n + k_2 + O(h^3)
 \end{aligned}
 \tag{30}$$

Symmetrization cancels out the first order term (which is shown in the error term) and makes the method a *second order* solver. A method is conventionally called *n*th order if its error term is  $O(h^{n+1})$ . In fact, Equation 30 above describes the second-order Runge-Kutta or midpoint method. There are many ways to evaluate the right-hand side  $f(x, y)$  that have different coefficients of higher-order error terms but lead to solutions that agree with those derived using a first order method. By choosing the optimal combination of right hand side terms, error terms can be systematically eliminated order by order. This is the basic idea of the Runge-Kutta method. The most commonly

employed method for numerical solutions is the fourth order Runge-Kutta formula because of its elegant organization that renders it easy to implement [15].

$$\begin{aligned}
 k_1 &= hf(x_n, y_n) \\
 k_2 &= hf\left(x_n + \frac{h}{2}, y_n + \frac{k_1}{2}\right) \\
 k_3 &= hf\left(x_n + \frac{h}{2}, y_n + \frac{k_2}{2}\right) \\
 k_4 &= hf(x_n + h, y_n + k_3) \\
 y_{n+1} &= y_n + \frac{k_1}{6} + \frac{k_2}{3} + \frac{k_3}{3} + \frac{k_4}{6} + O(h^5)
 \end{aligned} \tag{31}$$

The fourth-order Runge-Kutta method requires four evaluations of the right hand side per step  $h$ . This is almost always superior to the midpoint method. In fact, this method proves to be very effective when combined with an adaptive step size algorithm. Each step in a sequence of steps is treated identically in a Runge-Kutta method [15]. Prior behavior of a solution is not used in its propagation and this is justified mathematically since any point along the trajectory of an ordinary differential equation can serve as an initial point. This approach does not minimize computer time, and can fail for problems whose nature requires a variable/adaptive step size. Adaptive step size control helps minimize computing time and is discussed in detail in the next section [15].

#### *2.4.1 Adaptive Step Size*

Adaptive step size control is used to give better accuracy to a solution while minimizing computational effort. The basic idea is to take small steps in areas of rapid change and larger steps where the rate of change is slower [15]. This usually results in gains of efficiency that are ten to a hundred or more times faster than without adaptive



step size control. Implementation of adaptive step size control requires that the stepping algorithm signal information about its performance, and most important, an estimate of its truncation error. In a fourth-order Runge-Kutta method, a technique called step doubling is often used. Each step is taken twice, once as a full step, then, independently, as two half steps (Figure 2.7).

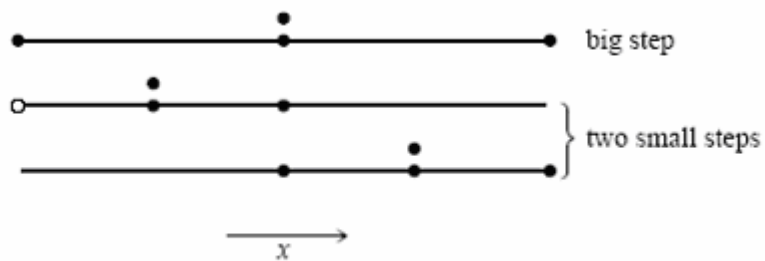


Figure 2.7 Step doubling as a means for adaptive step size control in fourth order Runge-Kutta. Points where the derivative is evaluated are shown as filled circles. The open circle represents the same derivative as the filled circle immediately above it, so the total number of evaluations is 11 per two steps. Comparing the accuracy of the big step with the two small steps gives a criterion for adjusting the step size on the next step, or for rejecting the current step as inaccurate [15].

Each of the three separate steps in the procedure requires 4 evaluations, however the single and double sequences share a starting point and thus the total number of evaluations required is 11. This should not be compared to 4, but rather to 8 evaluations (due to the two half-steps), since the accuracy of the half stepsize is achieved. The overhead cost is therefore a factor 1.375 [15].

To illustrate the advantage of this method, let us denote the exact solution for an advance from  $x$  to  $x + 2h$  by  $y(x + 2h)$  and the two approximate solutions by  $y_1$  (one

step  $2h$ ) and  $y_2$  (2 steps each of size  $h$ ). Since the basic method is fourth order, the true solution and the two numerical approximations are related by

$$\begin{aligned} y(x + 2h) &= y_1 + (2h)^5 \phi + O(h^6) + \dots \\ y(x + 2h) &= y_2 + 2(h^5)\phi + O(h^6) + \dots \end{aligned} \quad (32)$$

where, to order  $h^5$ , the value  $\phi$  remains constant over the step. In a Taylor series expansion,  $\phi$  represents a number whose order of magnitude is  $(y^{(5)}(x)/5!)$ . The first expression in Equation 32 involves  $(2h)^5$  since the step size is  $2h$ , while the second expression involves  $2(h^5)$  since the error on each step is  $h^5\phi$  [15]. The difference between the two numerical estimates gives the truncation error

$$\Delta \equiv y_2 - y_1 \quad (33)$$

The method aims to keep the truncation error to a desired degree of accuracy which is neither too large nor too small. This is realized by adjusting the step size,  $h$  [15]. Equation 32 can be solved by ignoring terms of order  $h^6$  and higher, to improve our numerical estimate of the true solution  $y(x + 2h)$ , namely,

$$y(x + 2h) \equiv y_2 + \frac{\Delta}{15} + O(h^6) \quad (34)$$

This estimate is accurate to the fifth order, one order higher than the original Runge-Kutta steps. Although the estimate is accurate to the fifth-order, the truncation error is not known at this stage. Therefore,  $\Delta$  is used as the error estimate. Such a procedure is called “local extrapolation” [15].

An alternative stepsize adjustment algorithm is based on the embedded Runge-Kutta formula, originally invented by Fehlberg. An interesting fact about Runge-Kutta

formula is that for orders,  $M$ , higher than four, more than  $M$  function evaluations (though never more than  $M + 2$ ) are required [15]. Thus the fourth-order method is often the first choice in numerical analysis problems. Fehlberg discovered a fifth-order method with six function evaluations where another combination of the six functions gives a fourth-order method. The difference between the two estimates of  $y(x + h)$  is used as an estimate of the truncation error to adjust the stepsize. Accordingly, embedded Runge-Kutta formulas, which are roughly a factor of two more efficient, have superseded algorithms based on step-doubling. The general form of a fifth-order Runge-Kutta formula is [15]

$$\begin{aligned}
k_1 &= hf(x_n, y_n) \\
k_2 &= hf(x_n + a_2h, y_n + b_{21}k_1) \\
&\dots \\
k_6 &= hf(x_n + a_6h, y_n + b_{61}k_1 + \dots + b_{65}k_5) \\
y_{n+1} &= y_n + c_1k_1 + c_2k_2 + c_3k_3 + c_4k_4 + c_5k_5 + c_6k_6 + O(h^6)
\end{aligned} \tag{35}$$

The embedded fourth-order formula and its corresponding error estimate are as follows

$$y_{n+1}^* = y_n + c_1^*k_1 + c_2^*k_2 + c_3^*k_3 + c_4^*k_4 + c_5^*k_5 + c_6^*k_6 + O(h^5) \tag{36}$$

$$\Delta \equiv y_{n+1} - y_{n+1}^* = \sum_{i=1}^6 (c_i - c_i^*)k_i \tag{37}$$

At this step, the approximate error is known and the next step is to keep the error within desired bounds. The error,  $\Delta$ , is proportional to the fifth power of the step size ( $\sim h^5$ ). If we take a step,  $h_1$ , and produce an error,  $\Delta_1$ , then the step  $h_0$  that would have given some other value  $\Delta_0$  is readily estimated as [15]

$$h_0 = h_1 \left| \frac{\Delta_0}{\Delta_1} \right|^{0.2} \quad (38)$$

Let  $\Delta_0$  denote the desired accuracy. Equation 38 is used in two ways: If  $\Delta_1$  is larger than  $\Delta_0$  in magnitude, the equation indicates how much to decrease the step size when the present (failed) step is retried. On the other hand, if  $\Delta_1$  is smaller than  $\Delta_0$ , then the equation can be used to determine the increment of the step size for the next step. Local extrapolation consists in accepting the fifth order value  $y_{n+1}$ , even though the error estimate actually applies to the fourth order value  $y^*_{n+1}$ . The desired accuracy,  $\Delta_0$ , is a vector, one for each equation in the set of ODEs. In general, all equations are assumed to be within their respective allowed errors. In other words, we will rescale the step size according to the needs of the equation with the worst error [15].

The next step is to relate the desired accuracy,  $\Delta_0$ , to some user defined error bounds. When dealing with a set of equations whose dependent variables differ enormously in magnitude, fractional errors are utilized (For example,  $\Delta_0 = \epsilon y$ , where  $\epsilon$  is the number like  $10^{-6}$ ). When dealing with oscillatory functions that pass through zero but are bounded by some maximum values,  $\Delta_0$  is set equal to  $\epsilon$  times the maximum values [15].

#### 2.4.2 Selection of Step Size

A well-known method for adjusting step size selection to the event functions is to include their first time derivative in the array of integrating variables. The extended system of differential equations can be written as

$$\frac{d}{dt} \begin{bmatrix} y \\ g \end{bmatrix} = \begin{bmatrix} f(y,t) \\ g(y,t) \end{bmatrix} \quad (39)$$

where  $y$  represents the state variables of the system, and  $g$  is an array collecting all active event functions. However, this measure alone does not suffice to warrant reliable event detection, because in a high order of the interpolation polynomials of the integrator, an even number of roots can occur within the integrator steps that remain undetected when simple sign checks are used [15].

#### 2.4.3 Continuous Interpolation Polynomials

Reliable event detection can be obtained by exploiting polynomials generated by the integrator for event functions in the extended system concurrently with a polynomial root finding algorithm to predict the number of roots contained in a single integration step [14]. However, standard interpolation polynomials of numerical integration codes often have the disadvantage of discontinuities at mesh points. Continuous extension interpolation polynomials that follow dense output formulas of [16] are employed in the Matlab routine (ode45) [17, 18] used in this research, to ensure continuity at the endpoints of an interval. The basic form of dense-output Runge-Kutta scheme is as follows

$$\begin{aligned} y_{n+1} &= y_n + h \sum_{i=1}^s b_i f_i \\ f_1 &= f(y_n, t_n) \\ f_i &= f(y_n + h \sum_{j=1}^{i-1} a_{ij} f_j, t_n + c_i h), i = 2, \dots, s \end{aligned} \quad (40)$$

A continuous extension can be computed using the same function evaluations,  $f_i$ , with

$$y_{n+1}^*(\sigma) = y_n + \sigma h \sum_{i=1}^{s^*} b_i^*(\sigma) f_i, \quad 0 \leq \sigma \leq 1, \quad (41)$$

where  $b_i^*(\sigma)$  are given polynomials of the interpolation parameter  $0 \leq \sigma \leq 1$  (see Table 2.2). The DOPRI5 scheme [19, 20] is a 7-stage explicit Runge-Kutta formula of fifth order with an embedded fourth order step for step size control. The fourth order continuous extension is used for the interpolation polynomials.

Table 2.2 RK5(4)7FM embedded pair (DOPRI5) [21]

$c_i$	$a_{ij}$						$\hat{b}_i$	$b_i$	$b_i^*$
0							$\frac{35}{384}$	$\frac{5179}{57600}$	$\frac{435\sigma^3 - 1184\sigma^2 + 1098\sigma - 384}{384}$
$\frac{1}{5}$	$\frac{1}{5}$						0	0	0
$\frac{3}{10}$	$\frac{3}{40}$	$\frac{9}{40}$					$\frac{500}{1113}$	$\frac{7571}{16695}$	$\frac{500\sigma(6\sigma^2 - 14\sigma + 9)}{1113}$
$\frac{4}{5}$	$\frac{44}{45}$	$-\frac{56}{15}$	$\frac{32}{9}$				$\frac{125}{192}$	$\frac{393}{940}$	$-\frac{125\sigma(9\sigma^2 - 16\sigma + 6)}{1113}$
$\frac{8}{9}$	$\frac{19372}{6561}$	$-\frac{25360}{2187}$	$\frac{64448}{6561}$	$-\frac{212}{729}$			$-\frac{2187}{6784}$	$-\frac{92097}{339200}$	$\frac{729\sigma(35\sigma^2 - 64\sigma + 26)}{1113}$
1	$\frac{9017}{3168}$	$-\frac{355}{33}$	$\frac{46732}{5247}$	$\frac{49}{176}$	$-\frac{5103}{18656}$		$\frac{11}{84}$	$\frac{187}{2100}$	$\frac{11\sigma(3\sigma - 2)(5\sigma - 6)}{84}$
1	$\frac{35}{384}$	0	$\frac{500}{1113}$	$\frac{125}{192}$	$-\frac{2187}{6784}$	$\frac{11}{84}$	0	$\frac{1}{40}$	$\frac{\sigma(\sigma - 1)(5\sigma - 3)}{2}$

## 2.5 Shooting Methods

In all but the simplest differential equations, an analytical solution is difficult to obtain and a numerical method is applied to solve the system. The shooting method is a numerical approach that is often used to deal with complex boundary value problems. Shooting to a fitting point is a symmetrical method and has the advantage of being readily applied to both linear and nonlinear differential equations using the same algorithm [22].

Shooting to a fitting point helps minimize the build-up of systematic error and is especially desirable in situations when a singularity is encountered in the differential equation. The simple shooting method is introduced and then built upon to give results for the "shooting to a fitting point" method which refines the prior method [22].

### *2.5.1 Simple Shooting Method*

In a simple shooting method, a differential equation in the form of  $y''(x)=F(y',y,x)$  with boundary conditions  $y(a)=\alpha$  and  $y(b)=\beta$  is solved. A solution for the boundary value problem is sought by guessing the slope of the solution  $y'(a)$  (refer to Figure 2.8).

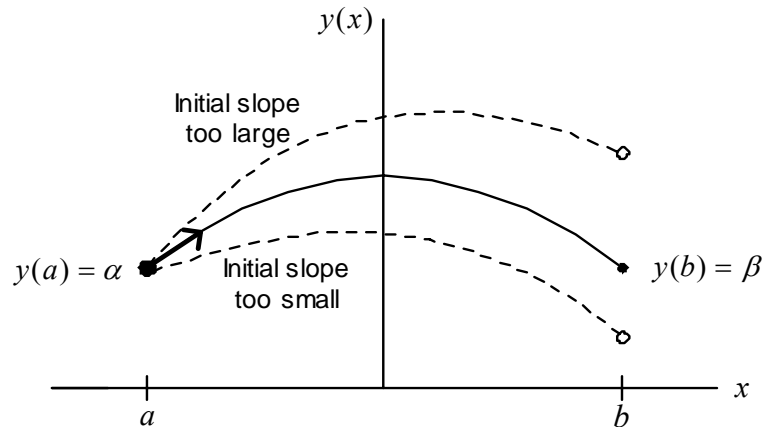


Figure 2.8 Method of shooting from an initial point  $x=a$  to  $x=b$ . Using initial an initial guess for the slope,  $y'(a)$ , the differential equation is numerically integrated from  $x=a$  to  $x=b$ . If the boundary condition,  $y(b)=\beta$ , is not satisfied, another initial slope,  $y'(a)$ , is tried until the boundary condition at  $x=b$  is satisfied[22].

This guess for the slope together with the known boundary condition,  $y(a) = \alpha$ , are used to numerically integrate the differential equation from  $x=a$  to  $x=b$ . When the solution does not satisfy the right boundary condition,  $y(b)=\beta$ , the slope at the left boundary,  $y'(a)$ , is varied until the right boundary condition is satisfied to some desired accuracy [22]. This simple shooting method works well for many problems but the method can fail if the integrating method (in this case, Runge-Kutta) is not able to perform the numerical integration through the whole region from  $x=a$  to  $x=b$ . This can happen because the differential equation has a singularity in the region of integration or because the end points of integration are singular and the numerical integration may fail when shooting into a singular point of the differential equation at  $x=b$ . Shooting to a fitting point also reduces the buildup of error and thus increases accuracy. The method



of shooting to a fitting point can be used as an effective alternative to overcome the drawbacks of the simple method of shooting [22].

### 2.5.2 Shooting to a Fitting Point

In this method, we integrate from the left boundary at  $x=a$  toward the right boundary at some intermediate fitting point,  $x_f$  where  $a < x_f < b$ . Next we integrate from the right boundary at  $x=b$  toward the left to the same intermediate fitting point,  $x_f$  (refer to Figure 2.9). This method is more symmetrical than the simple shooting scheme. Furthermore, when there are singularities at the boundary (such as in a singular Sturm-Liouville problem), we are shooting away from the singularities rather than into them.

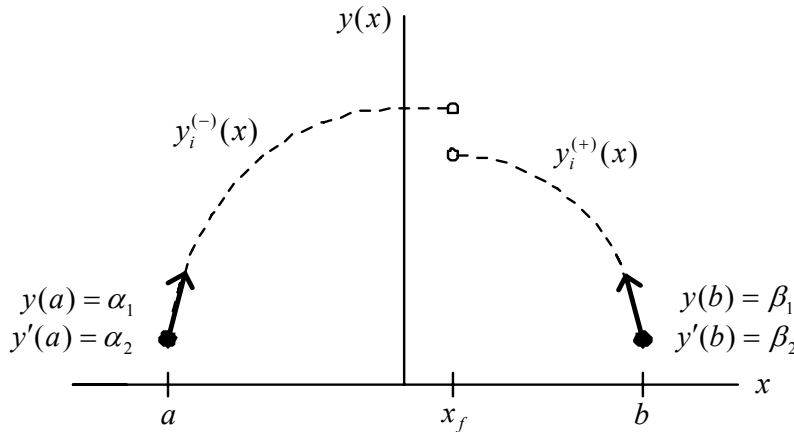


Figure 2.9 Shooting to an intermediate fitting point,  $x_f$ . This involves two numerical integrations, one starting at  $x=a$  and going to  $x=x_f$ , the other starting point at  $x=b$  and going to  $x=x_f$ . Both solutions and their derivatives must match at  $x=x_f$  [22].

Consider a boundary problem defined by the second order differential equation

$$\frac{d^2 y}{dx^2} = F(y', y, x) \quad (42)$$

with the boundary conditions,  $y(a)=\alpha_1$  and  $y(b)=\beta_1$ . Setting  $y_1(x)=y(x)$  and  $y_2(x)=y'(x)$  such a second order differential equation can be written as two first order equations [22]

$$\frac{dy_i}{dx} = f(y_1, y_2, x), \quad i = 1, 2 \quad (43)$$

with the boundary conditions,  $y_1(a)=\alpha_1$  and  $y_1(b)=\beta_1$ . In order to integrate the system of two first order equations from  $x=a$  to  $x=x_f$ , we must have two initial conditions,  $y_1(a)$  and  $y_2(a)$ . However only  $y_1(a)$  is known and a guess at the value of  $y_2(a)$  is made and the set of equations from  $x=a$  to  $x=x_f$  are numerically integrated . These functions are called  $y_i^{(-)}(x)$  for  $i=1,2$ . The situation on the right hand side of  $x_f$  is similar [22]. The slope of  $y_2(b)$  is not known and a guess is used during integration from  $x=b$  to  $x=x_f$ . These two functions are called  $y_i^{(+)}(x)$  for  $i=1,2$ . The solutions  $y_i^{(-)}(x)$  and  $y_i^{(+)}(x)$ , for  $i=1,2$ , must match at  $x=x_f$ . This is unlikely on the first try and therefore a discrepancy function,  $\Delta_i = y_i^{(-)}(x_f) - y_i^{(+)}(x_f)$  for  $i=1,2$  is constructed. The vector of the discrepancy function,  $\Delta_i$ , depends on two variables,  $\alpha_2 = y_2(a)$  and  $\beta_2 = y_2(b)$  , which are the two unknown slopes needed to construct a solution to the boundary value problem. These unknown slopes are found by searching for a simultaneous zero of the function,  $\Delta_i$ , for some value of  $\alpha_2$  and  $\beta_2$ . The solution to the boundary value problem is then found by using the slopes,  $\alpha_2$  and  $\beta_2$ , to integrate the system of equations from  $x=a$  to  $x=x_f$  and from  $x=b$  to  $x=x_f$  respectively [22].

In the general case, a boundary value problem consists of a set of 'N' first order differential equations

$$\frac{dy_i}{dx} = f_i(y_1, \dots, y_N, x), \quad i = 1, \dots, N \quad (44)$$

or an  $N^{\text{th}}$  order differential equation

$$\frac{d^N y}{dx^N} = F(y, y', \dots, y^{(N-1)}, x) \quad (45)$$

which can be rewritten as a set of  $n$  first order differential equations. Assume that there are  $n_1$  boundary conditions specified at  $x=a$  and  $n_2$  conditions at  $x=b$  so that  $n_1 + n_2 = N$ . Therefore,  $N$  initial conditions must be known in order to numerically integrate the system of  $N$  first order differential equations from  $x=a$  to some fitting point,  $x_f$ , where  $a < x_f < b$ . Consequently, guesses have to be made for  $n_2 = N - n_1$  initial conditions at  $x=a$ . [22] Similarly in order to numerically integrate the system of equations from  $x=b$  to  $x=x_f$ , guesses have to be made for values for  $n_1 = N - n_2$  initial conditions at  $x=b$ . An  $N$  component discrepancy function,  $\Delta_i = y_i^{(-)}(x_f) - y_i^{(+)}(x_f)$  for  $i=1, 2, \dots, N$ , is constructed which depends on the  $n_2$  free parameters at  $x=a$  and the  $n_1$  free parameters at  $x=b$ . The values of the  $N$  parameters that make the functions,  $\Delta_i$ , simultaneously zero give the initial conditions so that the system of  $N$  first order differential equations can be integrated numerically to yield the solution of the boundary value problem [22].

When either the boundary conditions are non-zero (e.g. non-zero  $\alpha_i$  or  $\beta_i$ ) or the differential equation is inhomogeneous, the boundary value problem is said to be inhomogeneous. Typically a well posed inhomogeneous boundary value problem has a unique solution. However the situation is different for Eigen value problems. A typical Eigen value problem is defined by a homogenous differential equation with homogenous boundary conditions (e.g.  $\alpha_i=0$  and  $\beta_i=0$ ) and does not have a unique solution. Instead it has a series of solutions (Eigen functions) that satisfy the boundary

conditions. Often Eigen value problems are more difficult to solve numerically than inhomogeneous boundary value problems. The reason for this increased difficulty is that in an Eigen value problem, there exist several unknown Eigen values and their corresponding Eigen functions rather than a single unique solution. This requires repetitive calculation to obtain all the desired Eigen functions and Eigen values [10, 22].

In this section the method of shooting to a fitting point is applied to solve a common Eigen value problem that arises in physical applications, namely the Sturm Liouville Eigen value problem [10]. This problem is defined by the differential equation

$$\frac{d}{dx} \left[ p(x) \frac{dy(x)}{dx} \right] - q(x)y(x) + \lambda r(x)y(x) = 0 \quad (46)$$

and the boundary conditions  $y(a)=0$  and  $y(b)=0$ . Here  $p(x)$ ,  $q(x)$ , and  $r(x)$  are real functions and  $r(x)$  is usually taken to be positive. The aim is to find a series of Eigen values,  $\lambda$ , and associated Eigen functions,  $y(x)$ . The Eigen value problem can be put into the form of a boundary value problem that is given by Equation 44 by treating the Eigen value,  $\lambda$ , as an unknown function which satisfies the differential equation,  $\lambda' = 0$ . Furthermore, since the differential equation is homogenous, if  $y(x)$  is a solution then so is  $cy(x)$  where  $c$  is a constant. It is conventional to choose the normalization of  $y(x)$  to be

$$\int_a^b r(x)y^2(x)dx = 1 \quad (47)$$

To enforce this normalization another auxiliary function,  $w'(x)$ , is introduced.

$$w'(x) = r(x)y^2(x) \quad (48)$$

Conventional normalization for  $y(x)$  is obtained by requiring that  $w(b)-w(a)=1$ . An arbitrary choice can be made for one of  $w(a)$  and  $w(b)$ . A transformation is made using Equation 49 to give the new functions  $y_1, y_2, y_3$  and  $y_4$ .

$$\begin{aligned}
 y_1 &= y \\
 y_2 &= p(x)y' \\
 y_3 &= \lambda \\
 y_4 &= w
 \end{aligned} \tag{49}$$

In terms of these functions the Eigen value problem can be written as [23]

$$\begin{aligned}
 y_1' &= \frac{1}{p(x)} y_2(x) \\
 y_2' &= q(x)y_1(x) - r(x)y_1(x)y_3(x) \\
 y_3' &= 0 \\
 y_4' &= r(x)y_1^2(x)
 \end{aligned} \tag{50}$$

with the boundary conditions [24]

$$\begin{aligned}
 y_1(a) &= 0 & y_1(b) &= 0 \\
 y_4(a) &= -r_0/2 & y_4(b) &= r_0/2
 \end{aligned} \tag{51}$$

where  $r_0$  is some convenient constant that determines the normalization of  $y(x) = y_1(x)$ .

In order to integrate the system of four differential equations (Equation 50), four initial conditions are needed. Integrating from the left boundary at  $x=a$  to fitting point at  $x=x_f$ , guess values for  $y_2(a)$  and  $y_3(a)$  are required. Similarly, integrating from the right boundary point at  $x=b$  to fitting point at  $x=x_f$ , guess values for  $y_2(b)$  and  $y_3(b)$  are needed. The discrepancy function,  $\Delta_i = y_i^{(-)}(x_f) - y_i^{(+)}(x_f)$ , will now have four components which depend on the four initial conditions,  $y_2(a), y_3(a), y_2(b),$  and  $y_3(b)$ . The solution to the boundary value problem can be obtained by choosing physically reasonable starting

values for the four initial conditions and searching for a zero of the discrepancy function,  $\Delta_i$  [22].

## 2.6 Simple Model: Undoped Case

The Ben Daniel-Duke Hamiltonian is used to study the behavior of electrons confined in quantum wells. This equation is also known as the modified Schrödinger's equation and can be solved with appropriate boundary conditions to give the wave functions and energy levels associated with electrons or holes [7,9]. The wave functions determine the probabilistic distribution of electrons or holes with respect to space. The general form of the Schrödinger equation for an electron is

$$-\frac{\hbar^2}{2m} \left( \frac{\partial^2}{\partial x^2} + \frac{\partial^2}{\partial y^2} + \frac{\partial^2}{\partial z^2} \right) \Psi + V(x, y, z) \Psi = E \Psi \quad (52)$$

where  $\hbar$  = reduced Planck's constant =  $\frac{6.626 \times 10^{-34}}{2\pi}$  Js ,  $m_0$  = mass of electron =  $9.1 \times 10^{-31}$  kg,  $V(x)$  = Potential energy,  $E$  = Energy of electron, and  $\Psi(x)$  = wave function.

In a semiconductor material, the mass  $m$  in the Schrödinger equation represents the effective mass rather than the bare electron mass and is a function of space for a particle under consideration [10]. In the case of quantum wells, wavefunctions and energy levels are confined in one direction and the modified Schrödinger's equation is:

$$-\frac{\hbar^2}{2} \frac{\partial}{\partial x} \frac{1}{m^*(x)} \frac{\partial}{\partial x} \Psi(x) + V(x) \Psi(x) = E \Psi(x) \quad (53)$$

where  $m^*(x) = m_e(x)m_0$  and  $m_e(x)$  is the effective mass of electron in the conduction band. The boundary conditions of  $\Psi(x)$  and  $\frac{1}{m^*(x)} \frac{\partial}{\partial x} \Psi(x)$  are continuous to avoid differentiating discontinuous functions which produces infinities [10]. A simple square well potential is give by

$$V_0 = \begin{cases} 0, & |x| < L_w / 2 \\ V_0, & |x| \geq L_w / 2 \end{cases} \quad (54)$$

where  $V_0$  is the barrier height and  $L_w$  is the well width. The functions in the Sturm Liouville problem of Equation. 46 are rewritten as

$$\begin{aligned} y(x) &= \Psi \\ p(x) &= \frac{\hbar^2}{2} \cdot \frac{1}{m^*(x)} \\ q(x) &= V(x) \\ \lambda &= E \\ r(x) &= 1 \end{aligned} \quad (55)$$

where 'r' is a constant function independent of  $x$ . It is convenient to introduce a length scale,  $x_0$ , defined by  $\hbar^2 / (m_0 x_0^2) = 1$  eV [9]. The length scale  $x_0 \approx 2.76042$  Å. Therefore Equation 55 can now be rewritten as

$$\begin{aligned} y(x) &= \Psi \\ p(x) &= x_0^2 \cdot \frac{1}{m_e(x)} \\ q(x) &= 2 \cdot V(x) \\ \lambda &= E \\ r(x) &= 2 \end{aligned} \quad (56)$$

## 2.7 Self Consistent Model: Doped Case

The theoretical methods described thus far have concentrated on solving systems for a single charge carrier. In many devices such models are inadequate especially when large numbers of charge carriers are present in the conduction band. The electrostatics describing the system is solved in order to decide whether typical carrier densities give rise to an additional potential over the band edge [25, 26].

### 2.7.1 Poisson Equation

Consider the case of an n-type material, where the number of free electrons in the conduction band is equal to the number of positively charged ionized donors in the heterostructure. In the example shown in Figure 10 six donors are ionized and supply six electrons into the well, thus maintaining charge neutrality.

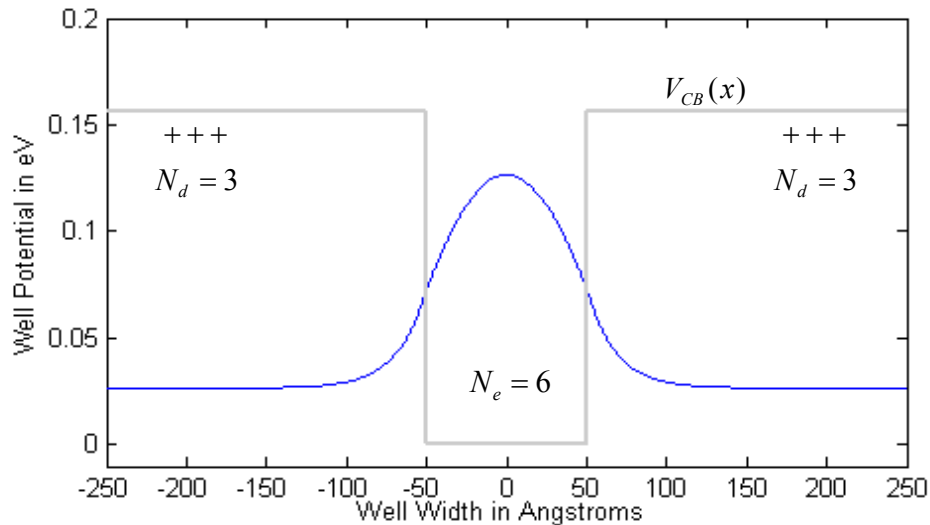


Figure 2.10 Modulation doped single quantum well [10]



Figure 2.10 is a modulation doped system and the doping is located in a position where free carriers it produces are spatially separated from the ions. The additional potential term,  $V_\rho(x)$ , which arises from this or any other charge distribution,  $\rho$ , can be expressed using Poisson's equation.

$$\nabla^2 V_\rho = -\frac{\rho}{\epsilon} \quad (57)$$

where  $\epsilon$  is the permittivity of the material that is  $\epsilon = \epsilon_0 \epsilon_r$ . The solution obtained via the electric field strength,  $\bar{E}$ , is given by

$$\bar{E}(x) = -\nabla V \quad (58)$$

and the potential is equal to

$$V_\rho(\bar{r}) = -\int_{-\infty}^{\bar{r}} \bar{E} \cdot d\bar{r} \quad (59)$$

If the potential profiles are one dimensional, they produce a one dimensional charge distribution [10]. In addition, quantum wells are assumed to be infinite in the x-y plane and hence any charge density,  $\rho(x)$ , can be assumed to be an infinite plane or a sheet with areal charge density,  $\sigma(x)$ , and thickness,  $\delta x$ , as shown in Figure 2.11.

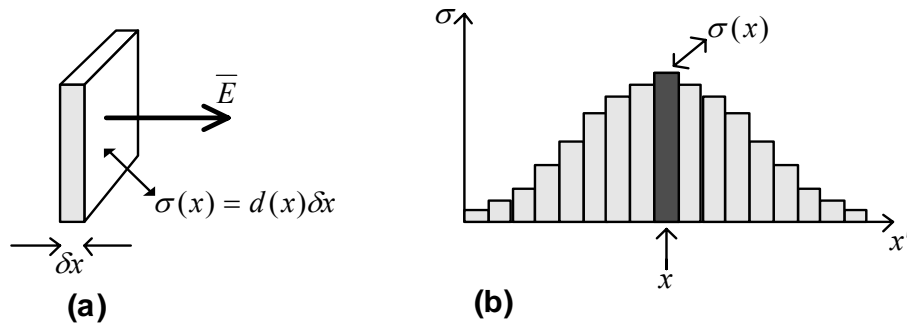


Figure 2.11 Electric field strength from an infinite plane of charge from a volume density of dopants,  $d(x)$  and thickness,  $\delta x$  [10]

Such an infinite plane of charge produces an electric field perpendicular to it with strength given by Equation 60.

$$\bar{E} = \frac{\sigma}{\epsilon} \quad (60)$$

Since the sheet is infinite in the plane, the field strength is constant at all distances from the plane. The total electric field strength due to many of these planes of charge, as shown in Figure 11(b), is then the sum of the individual contributions as follows

$$\bar{E}(x) = \sum_{x'}^{\infty} \frac{\sigma(x')}{\epsilon} \text{sign}(x - x') \quad (61)$$

where the function sign is defined as

$$\text{sign}(x) = +1, \quad x \geq 0; \quad \text{sign}(x) = -1, \quad x < 0 \quad (62)$$

This accounts for the vector nature of  $\bar{E}$ , i.e. if a single sheet of charge is at position  $x'$ , then for  $x > x'$ ,  $\bar{E}(x) = +\sigma/\epsilon$ , whereas for  $x < x'$ ,  $\bar{E}(x) = -\sigma/\epsilon$ . Moreover, there exists charge neutrality, i.e. there are as many ionized donors (or acceptors), in the system as there are electrons (or holes). This can be expressed mathematically as Equation 63 [10].

$$\sum_{x=-\infty}^{+\infty} \sigma(x) = 0 \quad (63)$$

It is the charge neutrality which ensures that the electric field and hence the potential, go to zero at large distances from the charge distribution. For the case of a doped semiconductor, there are two contributions to the charge density  $\sigma(x)$ , (i) ionized impurities and (ii) free charge carriers. Ionized impurities are known from the doping profile densities in each semiconductor layer as defined at growth time [10]. Free

charge carriers are calculated from the probability distribution of the carriers in the heterostructure. Thus if  $d(x)$  defines the volume density of the dopants at position  $x$ , where the planes are separated by the step length,  $\delta x$ , then the total number of carriers per unit cross sectional area, introduced in to the heterostructure is given by

$$N = \int_{-\infty}^{+\infty} d(x) dx \quad (64)$$

The net charge density in any of the planes is

$$\sigma(x) = q[N\Psi^*(x)\Psi(x) - d(x)]\delta x \quad (65)$$

where  $q$  is the charge on the extrinsic carriers. The step length,  $(\delta x)$ , selects the proportion of the carriers that are within the slab and converts the volume density of dopant,  $d(x)$ , into an areal density [27]. If the charge carriers are distributed over more than one subband, then the contribution to the charge density,  $\sigma(x)$ , would have to be summed over the relevant subbands (Equation 66).

$$\sigma(x) = q\left(\sum_{i=1}^n N_i \Psi_i^*(x)\Psi_i(x) - d(x)\right)\delta x \quad (66)$$

Figure 2.12 shows the areal charge density along the growth axis for a 100 Å GaAs well, n-type doped to  $1 \times 10^{18} \text{ cm}^{-3}$ , surrounded by 200 Å  $\text{Ga}_{0.8}\text{Al}_{0.2}\text{As}$  barriers.

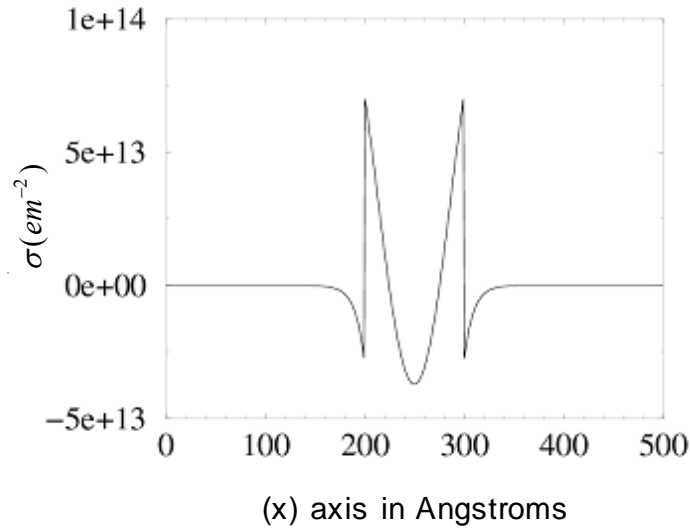


Figure 2.12 Areal charge density for a 100 angstrom GaAs well, n-type doped to  $1 \times 10^{18} \text{ cm}^{-3}$  surrounded by undoped  $\text{Ga}_{0.8}\text{Al}_{0.2}\text{As}$  barriers [10]

All the electrons introduced by doping are assumed to occupy the ground state of the quantum well. The ionized donors give rise to a constant contribution,  $\sigma$ , within the well of  $d(x)\delta x = 10^{24} \text{ m}^{-3} \times 10^{-10} = 10^{14} \text{ m}^{-2}$ , in each of the  $10^{10} \text{ m}$  thick slabs. The total number of  $N$  electrons in the quantum well is  $100 \times 1 \times 10^{14} \text{ m}^{-2} = 10^{16} \text{ m}^{-2}$ .

Figure 2.13 plots the electric field strength  $E$  due to the charge along the growth axis of the heterostructure.

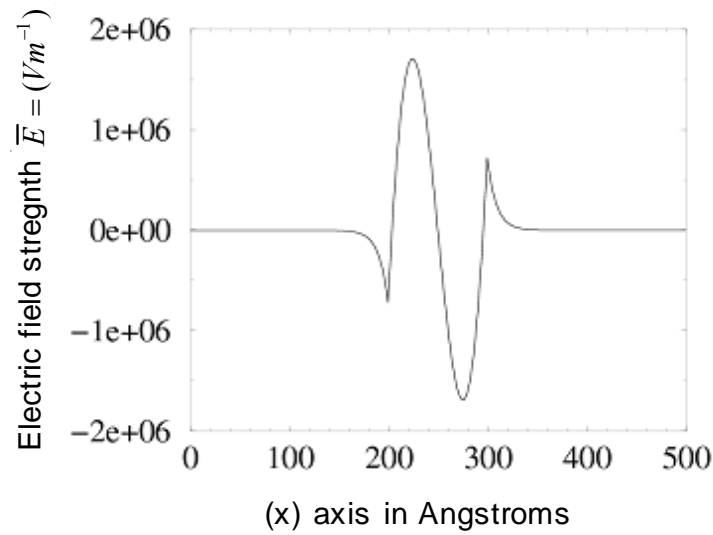


Figure 2.13 The electric field strength due to the charge distribution shown in figure 2.12[10]

The field reaches zero at either end of the structure implying charge neutrality. In addition, the symmetry of the charge distribution is reflected by the zero point in the center of the structure. The electric field strength is an intermediate quantity but the more significant quantity is the potential due to this charge distribution. Figure 2.14 plots the potential as calculated from Equation 59, by defining the origin for the potential at the left hand edge of the barrier well structure which is the effective infinity for the system under consideration.

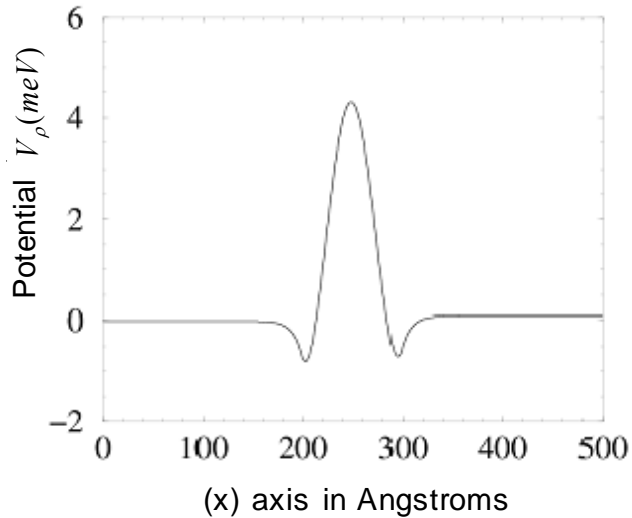


Figure 2.14 The potential due to the donor (electron) charge distribution[10]

Again, the symmetry of the original heterostructure and doping profiles are reflected in the symmetric potential. The potential is positive at the center of the well since the system consists of electrons in the conduction band, and any test charge used to probe the potential is also an electron which is repelled by the existing charge. The carrier density in the quantum well is reasonably high ( $\sim 10^{12} \text{ cm}^{-2}$ ) and produces a potential ( $\sim 4 \text{ meV}$ ) which is small compared to the conduction band offset (usually on the order of 100-200 meV). This potential can still have a measurable effect on the energy Eigen values of the quantum well [10].

### 2.7.2 Self Consistent Schrödinger Poisson Solution

Consider the introduction of a test electron into the system. The energy Eigen values are calculated by incorporating the potential due to the test electron with the

carrier density present into the standard Schrödinger equation i.e. the potential term,  $V(x)$ , in Equation 53 becomes [10]

$$V(x) \rightarrow V_{CB}(x) + V_{\rho}(x) \quad (67)$$

where  $V_{CB}$  represents the band edge potential at zero doping and the function,  $V_{\rho}$ , represents the potential due to the number of carriers, that is the charge density,  $\rho$  [9].

The numerical shooting method described earlier (refer to Section 2.5.2) can be used to solve for the new potential which yields new energies and wave functions. This is important since the potential due to the charge distribution depends on its wave functions. It is thus necessary to form a closed loop consisting of the following steps:

1. Solve the Schrödinger's equation
2. Calculate the potential due to the resulting charge distribution
3. Add the potential (step 2) to the original band edge potential
4. Solve Schrödinger's equation again with the new band edge potential (step 3)
5. Repeat until the energy Eigen values converge

This process is illustrated in Figure 2.15.

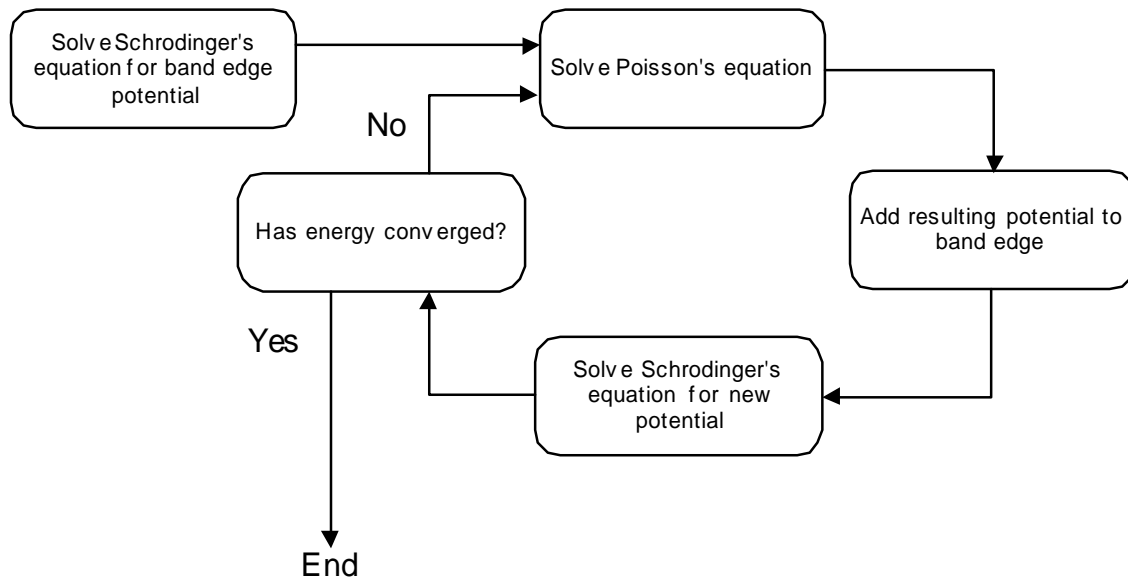


Figure 2.15 Block diagram of the iterative process used to solve the self consistent model [10]

At this point the wave functions are simultaneous solutions to both Schrödinger's and Poisson's equations and are described as the self consistent solution, like Hartree's approach to solving many electron atoms. Figure 2.16 shows the result of adding the potential due to the charge distribution,  $V_p$ , (refer to Figure 2.14) to the original band edge potential,  $V_{CB}$ , for a single quantum well. The perturbation (even at this high carrier density  $\sim 1e12 \text{ cm}^{-2}$ ) is relatively small compared to the barrier height but it is important to calculate the effect of this perturbation on the electron energy levels using the previously described iterative process to look for convergence of the resulting Eigen solutions.



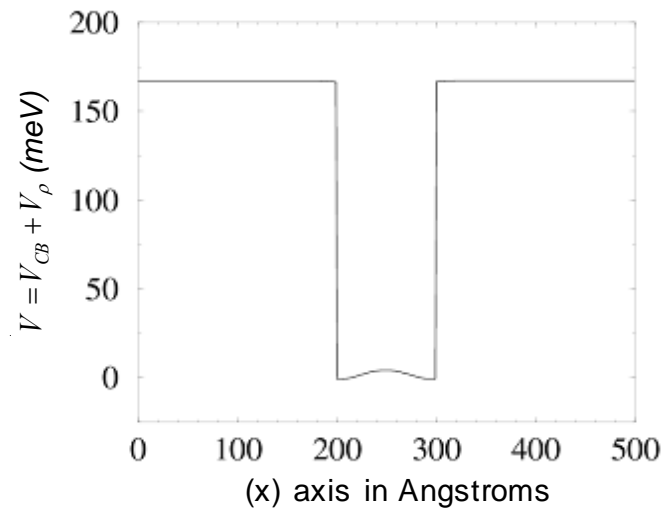


Figure 2.16 The sum of the band edge potential,  $V_{CB}$ , Poisson's potential,  $V_{\rho}$ , for the single quantum well of Figure 12 [10]

## CHAPTER 3

### QUANTUM-WELL USER ENTERED SIMULATION TOOL (QUEST)

**Q**uantum-well **U**ser **E**ntered **S**imulation **T**ool (**QUEST**) is a suite of simulation tools with an appealing and simple-to-use graphical user interface to solve the states, potentials and wave functions for user defined quantum well structures. The main purpose of building such an integrated system of tools is to simulate different structures before fabrication in the laboratory to test whether the structures look promising. If the wave functions, states and potentials are found to be acceptable after simulation than they can be made in the lab or discarded in the simulation stage and other materials or geometries can be tried till the desired results are obtained. Thus the solver is the first step to efficient time and money management in the device development process.

#### 3.1 Developing the Suite of Tools

The code was developed primarily in Matlab but also contains some modules written in C. After the code was developed and tested to remove bugs, error handling and a graphical user interface (GUI) was added. The GUI was created to make the program user friendly and efficient. The GUI was designed using dialog and indication boxes in Matlab. Furthermore the tools allows for the simulation of several structures in a single session. The results of each structure in a session can be stored to a different location. The result is a working tool to calculate states and wave functions for the

conduction band for an arbitrarily shaped quantum well that was input by the user. QUEST can be compiled into a stand-alone version for users who do not have Matlab available to them. This version is compatible with Windows 2000 and Windows XP operating systems. Future work will involve the extension of QUEST to calculate valence band states, potentials and wave functions in addition to handling excitons and the associated calculations.

### 3.2 QUEST Features

QUEST contains several features such as input dialog boxes, error handling and choice of data storage. These features are discussed in detail in this section.

#### *3.2.1 Input Features*

At start-up QUEST brings up the following interface (Figure 3.1), which contains eight fields for user input. The red numbers are not included in the original interface and have been added to the user manual figures to facilitate the explanation of each input field.

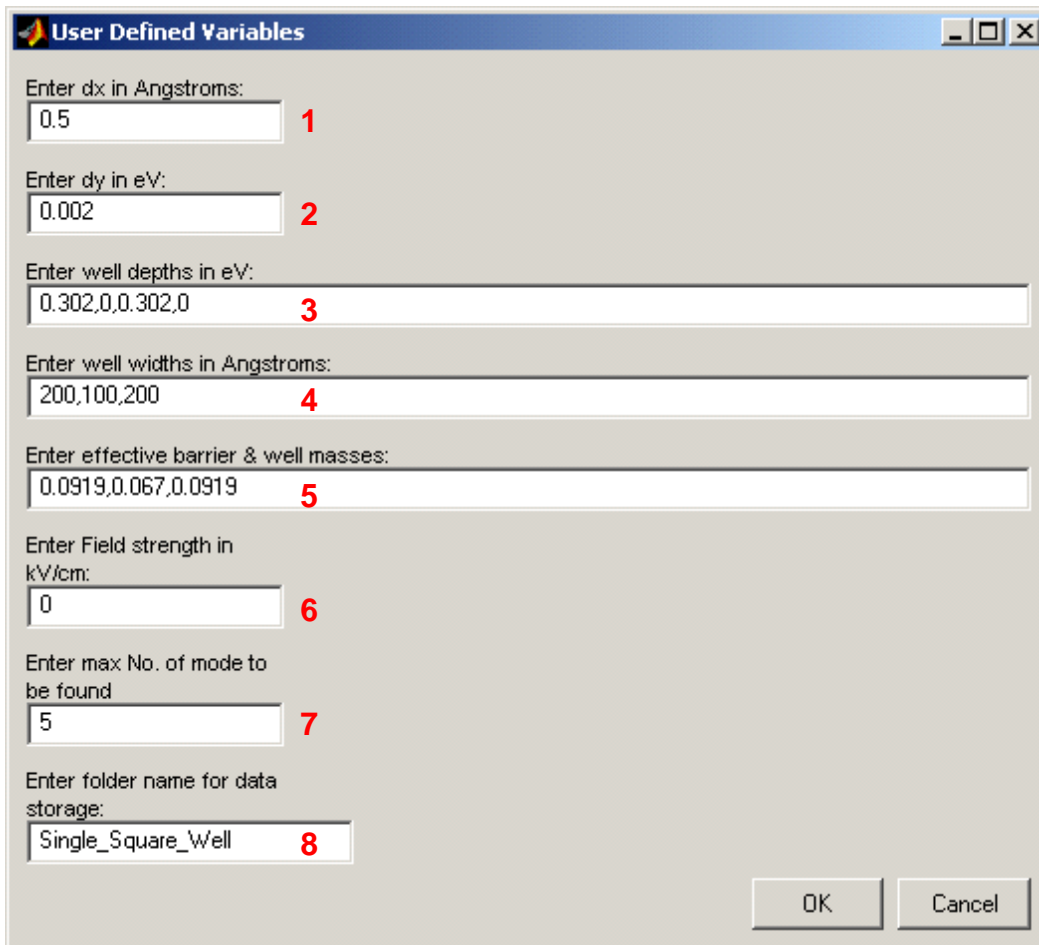


Figure 3.1 User Interface for QUEST at start-up

Input Field (1): "Enter dx in Angstroms"

This field defines the step-size used by the Runge-Kutta solver as defined along the x-direction/growth axis. Values of 'dx' that yield good results range from 0.1 to 1, with an optimal step-size of 0.5 for typical well structures. This value can be adjusted to change accuracy of calculation and computation time.

Input Field (2): "Enter dy in eV"

This field defines the step-size used by the Runge-Kutta solver as defined along the y-direction. Values of 'dy' that yield good results range from 0.001 to 0.005, with an optimal step-size of 0.002 for typical well structures. This value can also be adjusted to change accuracy of calculation and computation time.

Input Field (3): "Enter well depth in eV"

This field defines the conduction band potential for each layer of the well structure. Each input should be separated by a comma where the first input defines the well depth for the left-most layer and the last input represents the right-most layer of the well structure. Typical values of well depth that range from 0 to 1 eV. *Note: The number of layers in the well depth i.e. the number comma separated inputs must equal the number of well widths and effective masses as defined by input (4) and (5).*

Input Field (4): "Enter well widths in Angstroms"

This field defines the width for each layer along the growth axis (x-axis) of the user-defined well structure. Each input should be separated by a comma where the first input defines the well width for the left-most layer and the last input represents the width of the right-most layer of the well structure. Typical values of well width that range from 5 to 500. *Note: The number of layers in the well width i.e. the number comma separated inputs must equal the number of well depths and effective masses as defined by input (3) and (5).*

Input Field (5): "Enter Effective barrier and well masses"

This field defines the effective masses for each layer along the growth axis (x-axis) of the user-defined well structure. Each input should be separated by a comma where the first input defines the effective mass for the left-most layer (usually a barrier) and the last input represents the effective mass of the right-most layer of the well structure (also usually a barrier) and the middle numbers represent either barriers or wells. Typical values of well width that range from 0.033 to 0.15 depending on the material to be simulated. *Note: The number of effective masses i.e. the number comma separated inputs must equal the number of well widths and well depths that define the number of layers in the structure as defined by input (3) and (4).*

Input Field (6): "Enter Field strength in kV/cm"

This field defines the external applied electric field at the center of the well. Typical values of applied electric field that range from -100 to 100 depending on the input well structure.

Input Field (7): "Enter max no. of modes to be found"

This field defines the upper limit on the number of modes/solutions that will be calculated for the well structure defined by the previous inputs. If this input exceeds the number of modes that can be excited in the defined well structure then all the possible modes will be calculated and displayed. The solver starts by finding the lowest energy mode and progresses to higher modes of increasing energy.

### Input Field (8): "Enter folder name for data storage"

This field defines the name of the folder in which all the output data folders and files will be stored. This folder does not have to be a pre-existing folder but it is created by QUEST for data storage when the simulator is run. The data folder is created in the root directory of the QUEST simulator which is the same location in which the program is stored and run from. The path for the folder is usually defined as follows DRIVE: \QUEST\wavefuncdata\Caution: If there exists a folder name that shares the user input folder name in this field then the folder and all data in it is overwritten by QUEST.

### 3.2.2 Error Handling

If the data entered by the user does not comply with the aforementioned format (For example: QUEST finds an alphanumeric string entered where numeric values are expected or unequal number of inputs is encountered in Inputs 3, 4 and 5) then the error message (Figure 3.2) is displayed on the screen to inform the user to check all inputs and make necessary changes.

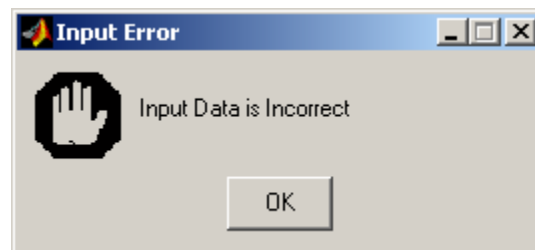


Figure 3.2 Error message displayed for incorrect input data

### 3.2.3 Running the Program

While the program is conducting the computations, a progress bar appears on the screen to inform the user of the extent of the calculations (Figure 3.3). This helps the user estimate the approximate computation time that is left to complete the simulation.



Figure 3.3 Progress bar while program is busy

Once the program is done calculating the solutions to the user input structure, the states and wavefunctions are displayed in a figure. After this step is complete, the user has results displayed for each solution that is asked for in a graphical format. Next the program brings up a dialog box that asks the user if another structure is to be simulated in the current session (Figure 3.4). If the user responds with a 'YES' to this question then the first dialog box where well specifications can be entered comes up again (Figure 3.1). The user can then proceed with entering specifications for the next well structure that has to be simulated. If the user responds with a 'NO' to this question then the next dialog box comes up (Figure 3.5).



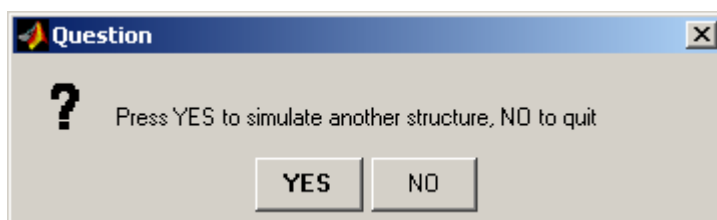


Figure 3.4 Dialog box to proceed to next structure or go to next step

The next dialog box queries the user about his next choice for the solution. If the user replies with a 'NO' to the question (Figure 3.5) then QUEST exits. However, if the user answers with a 'YES' then the program proceeds to the next step for the Poisson Self-consistent model.

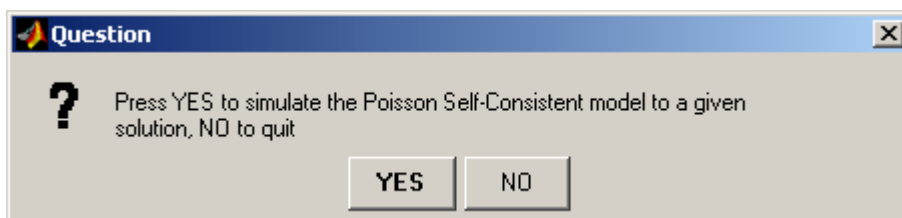


Figure 3.5 Dialog box to proceed to the Poisson self-consistent model

At this point the user has decided to carry out the calculations for the Poisson Self-consistent model and an input dialog box comes up to prompt the entry of variables that define the doping structure of the well structure that has been simulated in the previous section. This interface (Figure 3.6) contains three fields for user input. The red numbers are not included in the original interface and have been added to the user manual figures to facilitate the explanation of each input field.

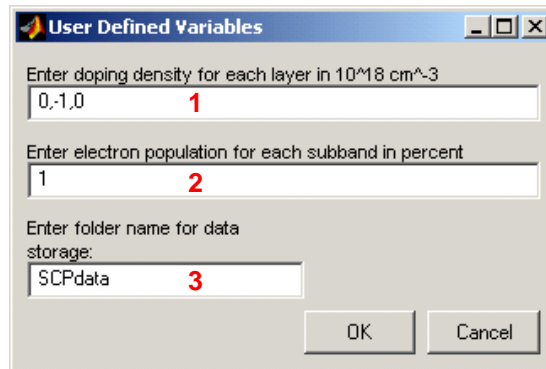


Figure 3.6 User defined variables for the Poisson self-consistent model

Input Field (1): "Enter doping density for each layer in  $10^{18} \text{ cm}^{-3}$ "

This field defines the doping density in each layer. Each input should be separated by a comma. The first input defines the doping density along the growth axis for the left-most layer (usually a barrier) and the last input represents the doping density of the right-most layer of the well structure (also usually a barrier) while the middle numbers represent either barriers or wells. It should be noted that negative values indicate doping with donors (e.g. Phosphorus that produces n-type material) and positive values indicate doping with acceptors (e.g. Boron that gives rise to a p-type material). (In this thesis, only calculations dealing with electrons are carried out that is conduction band calculations have been implemented and hence all values entered for doping density will always be negative numbers. This field can be modified to hold positive values for future work that includes calculations for holes). Values of doping density vary widely depending on the well structure and should be chosen carefully to

conform to the desired material and geometry of the well structure to be simulated while being practical and capable of generating viable solutions. *Note: The number of doping density entries i.e. the number comma separated inputs must equal the number of well widths, well depths and effective masses that define the number of layers in the structure as defined by input (3), (4) and (5) in the first dialog box(Figure 17). If not, the program will generate an error and exit.*

Input Field (2): "Enter electron population for each subband in percent"

This field specifies the proportion of charge carriers (in this case, electrons) in each of the quantum well energy levels, that is the percentage of the total are input for each energy level (e.g. For a population of electrons split over two lowest energy levels can be given 60, 40 to represent that 60% of the total carrier population is in the first energy level and the remaining 40% is in the next level). To further clarify, the two files picked in Figure 3.7 define the two energy levels that will be considered in this step. The first wave function file relates to the lowest energy level and thus the first number input into this field while the second wave function file corresponds to the higher energy level and the second number entered by the user in to field (2). If a single number (100) is entered instead of two numbers then the configuration assumes that electrons introduced by the doping all occupy the ground state of the quantum well and thus there is no contribution to the higher energy level. Values of 'electron population in percent' range from 0 to 100 corresponding to no contribution of doping to that level and to all contribution of doping to that level only, respectively.

Input Field (3): "Enter folder name for data storage"

This field defines the name of the folder in which all the output data folders and files are stored. This folder does not have to be a pre-existing folder. It is created by QUEST for data storage when the simulator is run. The data folder is created in the root directory of the QUEST simulator which is the same location that the program is stored in and run from. The path for the folder is usually defined as follows DRIVE: \QUEST\wavefuncdata\Caution: If there exists a folder name that shares the user input folder name in this field then the folder and all data in it is overwritten by QUEST.

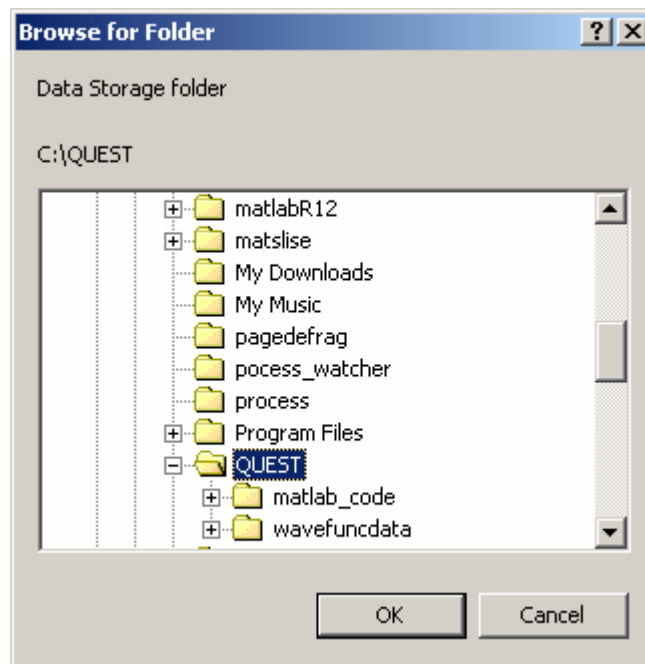


Figure 3.7 'Browse for folder' selection box

After the user completes the input fields in the dialog box shown in Figure 3.6 and clicks 'OK', QUEST brings up a 'Browse for folder' selection box (Figure 3.7). By default the QUEST root directory is selected. The user is given the option to choose the directory where previous calculations for the input well structure are stored. This allows the user to pick between any well structures that may have been simulated at an earlier time. The user is advised to choose the folder containing the states and wave functions data for the well.

#### *3.2.4 Flow Chart of QUEST Hierarchy*

The following flow chart (Figure 3.8) shows the various components/programs of QUEST. Each program is represented by a box and the arrows interconnecting the boxes show the functionality dependence of the interacting components. A short description of each program, its layout, functionality and input/output files is outlined next.

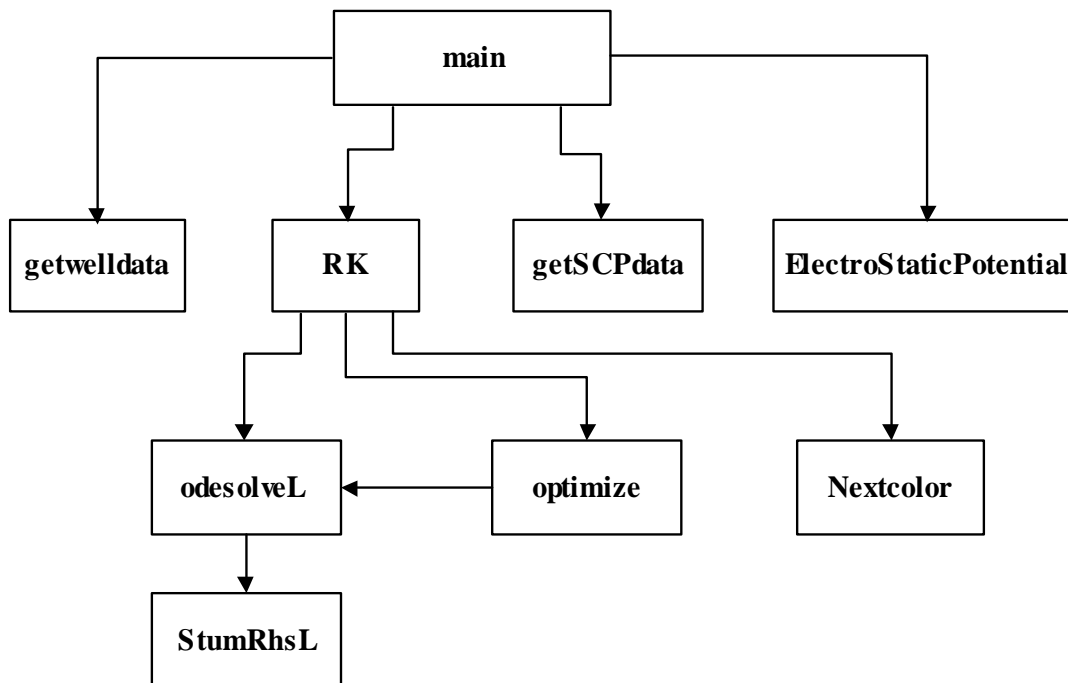


Figure 3.8 Flow chart representing the QUEST hierarchy

### Function 1 (main)

The 'main' function is the entry point of the QUEST program and the tool begins execution at the function 'main'. When QUEST is compiled and run, the code that is first executed is the code within the function titled 'main'. This function calls the following functions: getwelldata, RK, getSCPdata and ElectrostaticPotential.

### Function 2 (getwelldata)

This function creates the first input dialog box as shown in Figure 3.1 and accepts all the user defined parameters for the well structure and auxiliary inputs (such as number of solutions needed, folder name for data storage) that are used in the

simulation. This function creates a file called 'userdata.txt' that stores the most recent user inputs.

This function name is an abbreviation that stands for Runge-Kutta. This name is chosen since this method for solving the differential Schrödinger equation for the well structure defined by the parameters in 'getwelldata'. This function defines the well structure in a .mat file called 'structure.mat'. This structure is divided into sections along the well depth. The thickness of each section is defined by the user in 'getwelldata' in the Field 2, 'dy'. RK then calls the next function 'odesolveL' which solves the differential equation (details in Function 6: odesolveL). As described in Section 2.5.2 (Shooting to a Fitting Point), the idea is to divide the total integration interval  $[a, b]$  into two parts,  $[a, x_f]$  and  $[b, x_f]$  where  $a < x_f < b$ . An integration algorithm is used to integrate within the two sub-intervals from the endpoints  $x=a$  and  $x=b$  towards the common match point  $(x_f)$ , using some guessed value for the energy,  $E$ . The next step is to determine if the guessed value of  $E$  is an Eigen value. When solving the Schrödinger equation in two separate regions, it is required that the wavefunction and its derivative are continuous at the common point.[27] If the solutions in the two sub-intervals are labeled as A and B, the matching condition becomes

$$\psi_A(x_f, E) = \psi_B(x_f, E) \text{ and } \frac{\psi'_A(x_f, E)}{m_A^*} = \frac{\psi'_B(x_f, E)}{m_B^*} \quad (67)$$

These two conditions can be combined into one equation as shown in Equation 68 where the expression on each side is referred to as the logarithmic derivative.

$$\frac{\psi'_A(x_c, E)}{m_A^* \psi_A(x_c, E)} = \frac{\psi'_B(x_c, E)}{m_B^* \psi_B(x_c, E)} \quad (68)$$

If the wave function has a node at the match point, both sides can be inverted, since it is unlikely that the derivative is zero. This condition holds exactly if  $E$  is an Eigen value. Further more, if a function is zero at some point, it should have different signs on opposite sides of this point (other than in a trivial case such as  $f(x)=x^2$  around  $x = 0$ ). Thus the aforementioned condition taken as a postulate and the function described in Equation 69 is assumed to change sign at the Eigen value. The Eigen values can thus be found using two major steps: first, integrate the differential equation for a number of different values of  $E$  (say an array covering the energy interval of interest), and second, find the zeros of  $f(E)$  by bracketing [27].

$$f(E) = \frac{\psi'_A}{m_A^* \psi_A} - \frac{\psi'_B}{m_B^* \psi_B} \quad (69)$$

A practical and simple way to perform this task is not to study the function  $f(E)$  but only record whether it is positive or negative to avoid the risk of dividing by zero [27].

$$g(E) = m_A^* \psi'_A \psi_B - m_B^* \psi'_B \psi_A \quad (70)$$

Similar to Equation 69, Equation 70 also changes sign around the Eigen value. In this way, an Eigen value is located with  $g(E) > 0$  on one side and  $g(E) < 0$  on the opposite. Next a standard routine for bracketing the roots of the equation  $g(E)$  to desired accuracy is employed. This bracketing procedure is implemented in Function 7 (optimize) [27].

The procedure described above is used repetitively to find all the Eigen values for the user-defined well structure. The method is implemented such that it searches for solutions starting from the lowest energy level of the well (bottom of the conduction band potential) and progresses incrementally along the well energy to the top of the



conduction band potential. Next the potential well, the Eigen values (states) and their corresponding wavefunctions are plotted.

The function also makes two output files in which the calculated data is stored. The first file stores the Eigen value/modes of the well structure and the second file holds the wavefunctions that correspond to each solution. The calculated Eigen values are stored in ASCII format. The stored file consists of two columns; the first column in the file represents the solution number/mode and the second column represents the Energy Level/Solution (Units: eV) of the well structure. The stored file is located in the QUEST root directory in a folder called 'wavefuncdata\*<user-defined-folder>*\Energy-Levels.rtf'. The *<user-defined-folder>* is the folder name input by the user in the first dialog box that comes up when QUEST is run (Refer to Figure 3.1, Field (8): "Enter folder name for data storage").

The wavefunctions that relate to the Eigen values are also calculated and stored in ASCII format. The stored file is located in the QUEST root directory in a folder called 'wavefuncdata\*<user-defined-folder>*\PSI*<solution\_no>*.dat'. The *<user-defined-folder>* is the folder name input by the user in the first dialog box that comes up when QUEST is run (Refer to Figure 3.1, Field (8): "Enter folder name for data storage"). The *<solution\_no>* indicates the number of the mode/Eigen value that the stored wavefunction corresponds to. The stored file consists of two columns; the first column in the file represents the growth axis /x-axis (Units: meters) and the second column represents the wave function (Normalized Units).

#### Function 4 (getSCPdata)

This function creates the second input dialog box as shown in Figure 3.6 and accepts all the user defined parameters for the doping profile and subband populations and the name of the folder for data storage. This function creates a file called 'SCPdata.txt' that stores the most recent user inputs.

#### Function 5 (ElectrostaticPotential)

This function reads in the states from a file ('Energy-Levels.rtf') in the user chosen folder. The stored file is located in the QUEST root directory in a folder called 'wavefuncdata\*<user-defined-folder>*\Energy-Levels.rtf'. The *<user-defined-folder>* is the folder chosen by the user in a dialog box (Refer to Figure 3.7, 'Browse for folder' selection box). Next the wave functions are read in from a file located in the QUEST root directory in a folder called 'wavefuncdata' which is located in 'wavefuncdata\*<user-defined-folder>*\PSI*<solution\_no>*.dat' (Refer Figure 3.6). The *<user-defined-folder>* is the same folder as described above. The *<solution\_no>* indicates the number of the mode/Eigen value that the stored wave function corresponds to. The stored ASCII file consists of two columns; the first column in the file represents the growth axis /x-axis (Units: meters) and the second column represent the wave function (Normalized Units). The function then proceeds to build the doping structure defined by the user (Refer Figure 3.6) and calculates the net areal charge, the electric field distribution and the potential due to the charged carriers,  $V_\rho$  (in this case electrons since QUEST in the present version performs calculations only for the conduction band). It returns the value

of  $V_p$  which is added to  $V_{CB}$  and the process is repeated until a solution is found within acceptable error bounds.

The final solution is stored in the following directory path (which is the root directory of QUEST by default) `DRIVE:\QUEST\wavefuncdata\<Folder_name>\<user-defined-folder>` where `<Folder_name>` is the folder chosen by the user in a dialog box (Refer to Figure 3.7, 'Browse for folder' selection box) and `<user-defined-folder>` is the name input by the user in the input dialog box (Refer Figure 3.6:User defined variables for the Poisson Self-consistent model). The naming convention and file format (Eigen values and wave functions) for the final solutions are the same as previously described.

#### Function 6 (odesolveL)

The inputs to this function are the parameters that describe the user defined well structure. This function uses the inbuilt Matlab function '*ode45*' to solve the given differential equation. '*ode45*' is based on an explicit Runge-Kutta (4,5) formula, the Dormand-Prince pair [17]. It is a one-step solver that is when computing  $y(t_n)$ , it needs only the solution at the immediately preceding time point,  $y(t_{n-1})$  and thus '*ode45*' is the best function to apply as a "first try" for most problems [14, 17]. The function '*odesolveL*' uses '*ode45*' to shoot towards the fitting point ( $x=x_f$ ) first from the right end point ( $x=b$ ) and then from the left end point ( $x=a$ ) (Refer to Section 2.5.2: Shooting to a fitting point). Next the derivatives at the fitting point ( $x=x_f$ ) are calculated. Finally, the function returns the left and right half of the wave function and the value of Equation 70. This function is called by Function 3 (RK) and Function 7 (optimize).

### Function 7 (optimize)

This function is called by the function '*fminbnd*' within Function 3 (RK). '*fminbnd*' is a standard routine for bracketing that can be used to minimize a function of one variable on a fixed interval. The algorithm is based on a Golden Section search and parabolic interpolation method [17]. This function is used by QUEST primarily to bracket the roots of the equation,  $g(E)$ , to desired accuracy (Refer Function 3-RK). The function '*optimize*' returns the value of  $g(E)$  and the complete/concatenated wave function ( $\Psi$ ) after a solution is found within acceptable error.

### Function 8 (nextcolor)

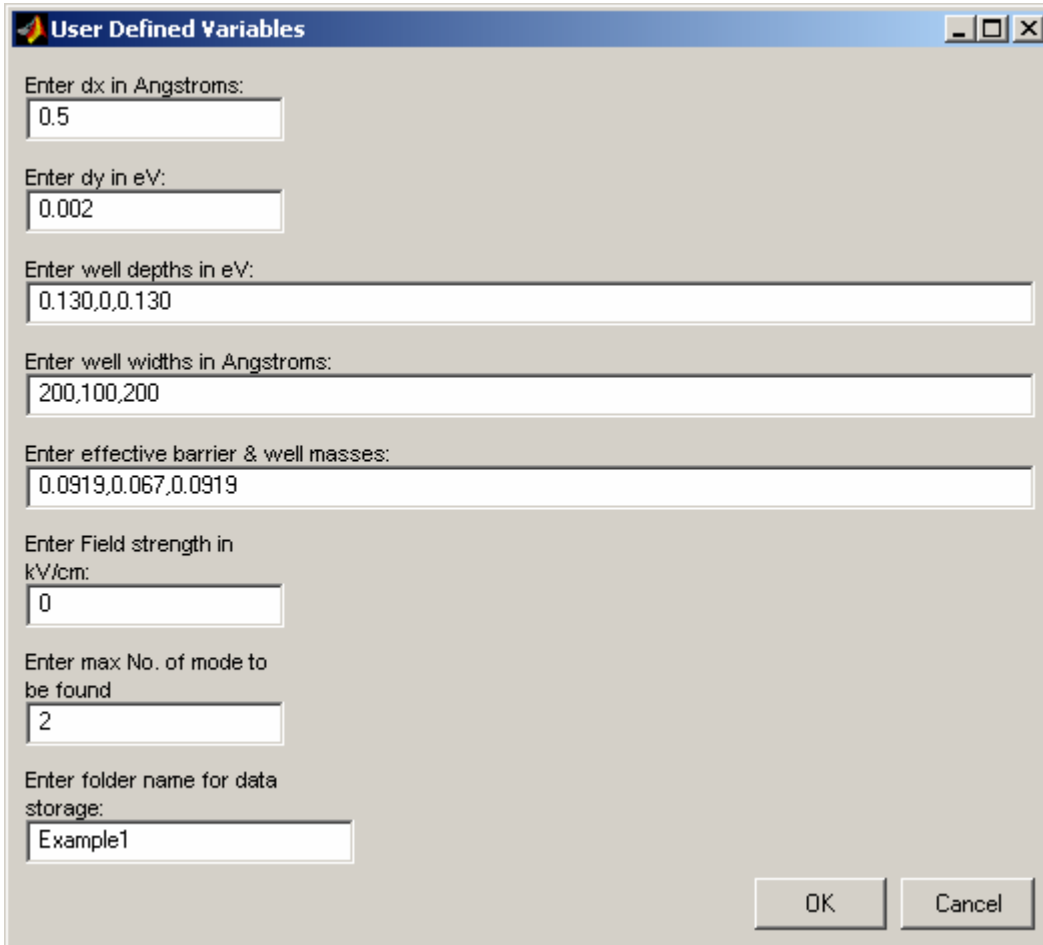
QUEST outputs graphs with multiple data traces (e.g. several wave functions plotted in the same figure). Each data trace is plotted using a different color. These colors are generated by the function '*nextcolor*'. This function returns the next value of the 'rgb' array that defines the color to be used in the plotting function as follows `plot(...,'Color', [r g b])`. The input vector '*rgb\_ip*' is a 1x3 vector of RGB values, each in the range of 0 to 1. This input vector is incremented by a predefined amount to give the output vector '*rgb\_op*', the final RGB vector [r g b] used during plotting. For example, with `rgb_ip=001` and `increase=1`, the `rgb_op` is 010.

### Function 9 (SturmRhsL)

This function defines the Schrödinger equation in a Sturm-Liouville form as four first order differential equations (Refer to Section 2.6 Simple Model: Undoped Case). This function is called by Function 6 (odesolveL).

### 3.3 Example of a Complete QUEST Run

In the following section two wells of different input parameters are run (Example 1 and Example 2). The well structure that is simulated in Example 2 is chosen for further calculations using the self consistent model. Results and intermediate steps are shown below to give the user an idea of what a complete run of QUEST looks like along with the types of graphs and results one can expect.



The image shows a Windows-style dialog box titled "User Defined Variables". It contains several input fields for defining parameters for a well structure. The fields are arranged vertically and include labels and text boxes. At the bottom right, there are "OK" and "Cancel" buttons.

Label	Value
Enter dx in Angstroms:	0.5
Enter dy in eV:	0.002
Enter well depths in eV:	0.130,0,0.130
Enter well widths in Angstroms:	200,100,200
Enter effective barrier & well masses:	0.0919,0.067,0.0919
Enter Field strength in kV/cm:	0
Enter max No. of mode to be found	2
Enter folder name for data storage:	Example1

Figure 3.9 Input screen for Example 1- first well structure

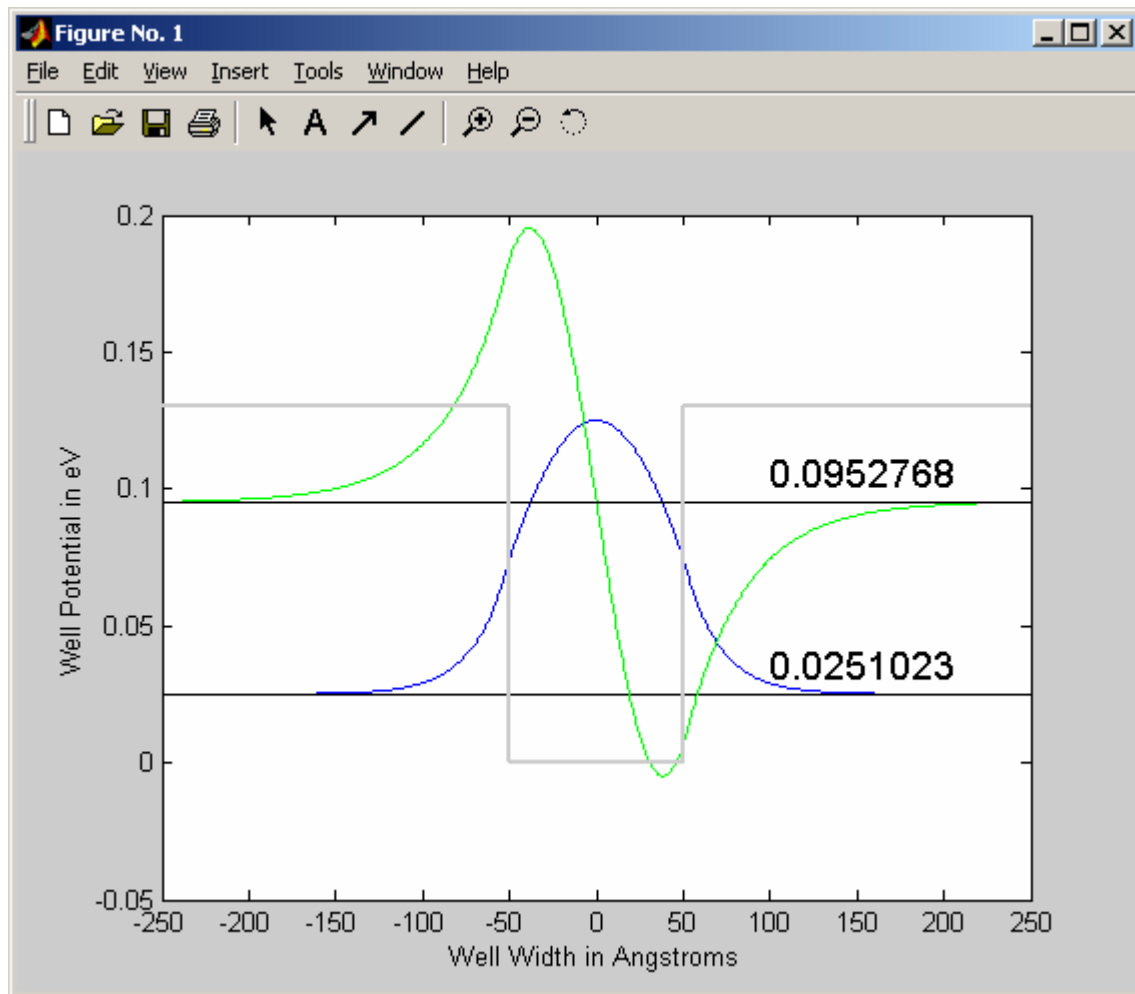


Figure 3.10 Output screen 1- Example 1 solutions (energy levels and wavefunctions)

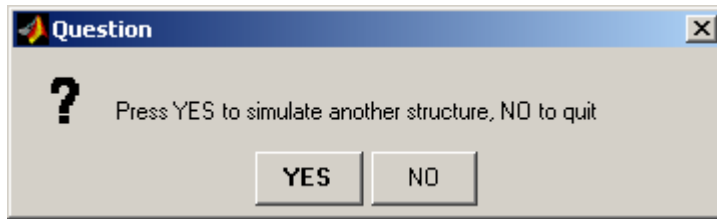


Figure 3.11 User chooses to simulate another well by clicking 'YES'

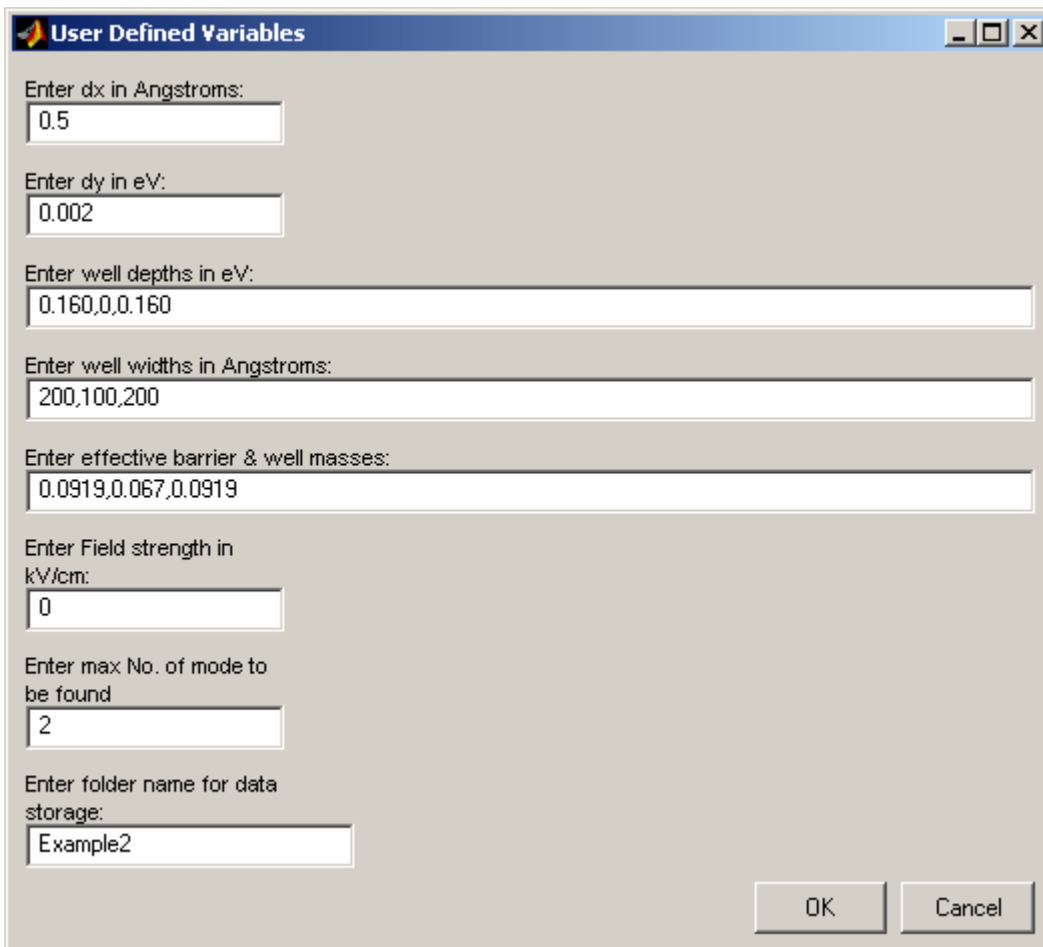


Figure 3.12 Input screen for Example 2- Second well structure



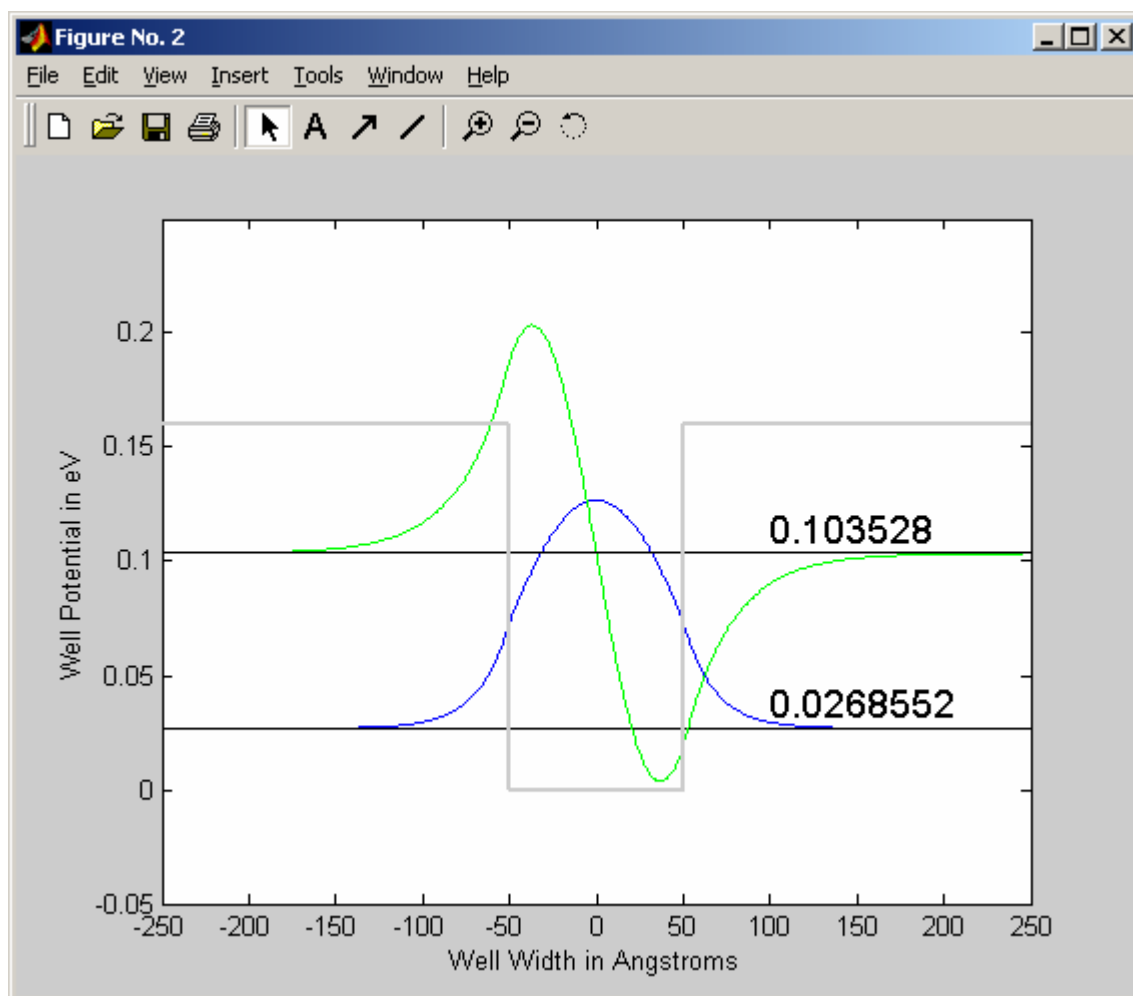


Figure 3.13 Output screen 2- Example 2 solutions (energy levels and wavefunctions)

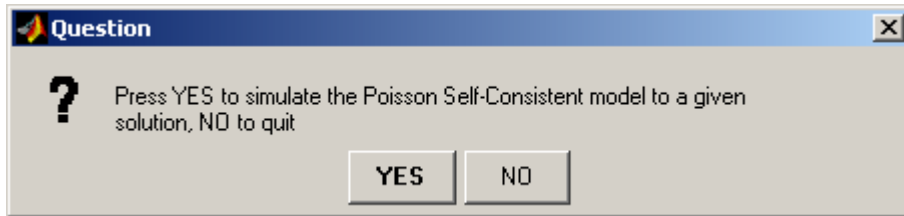


Figure 3.14 User chooses to continue with the Self consistent model by clicking 'YES'

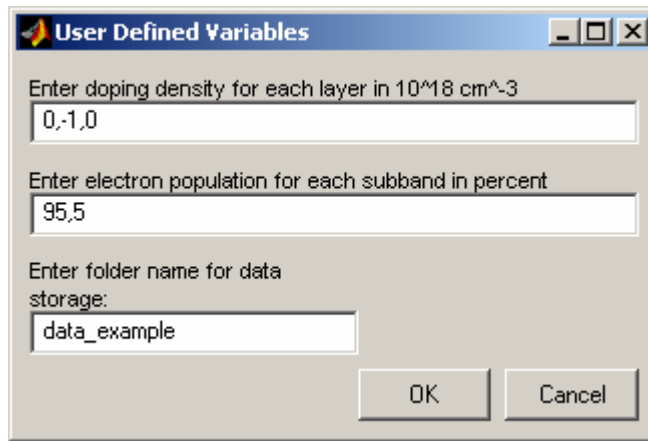


Figure 3.15 Input screen for Example 2- doping structure

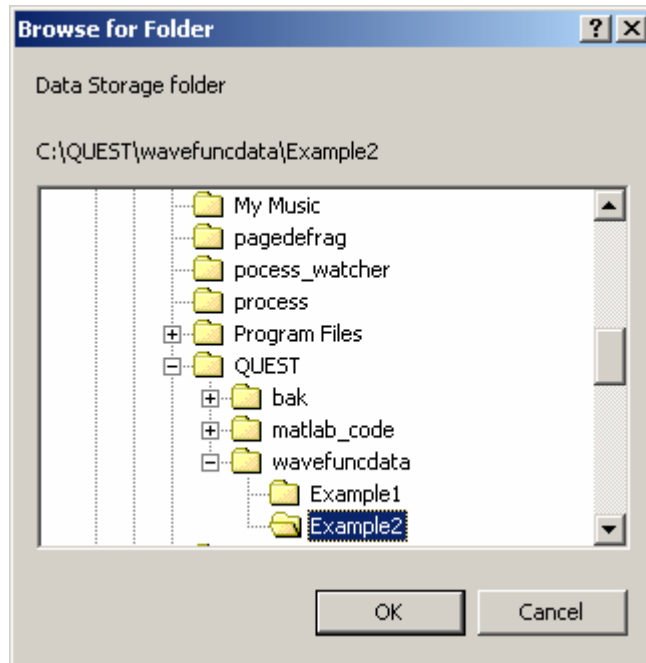


Figure 3.16 User chooses the well for further calculations (here Example 2)

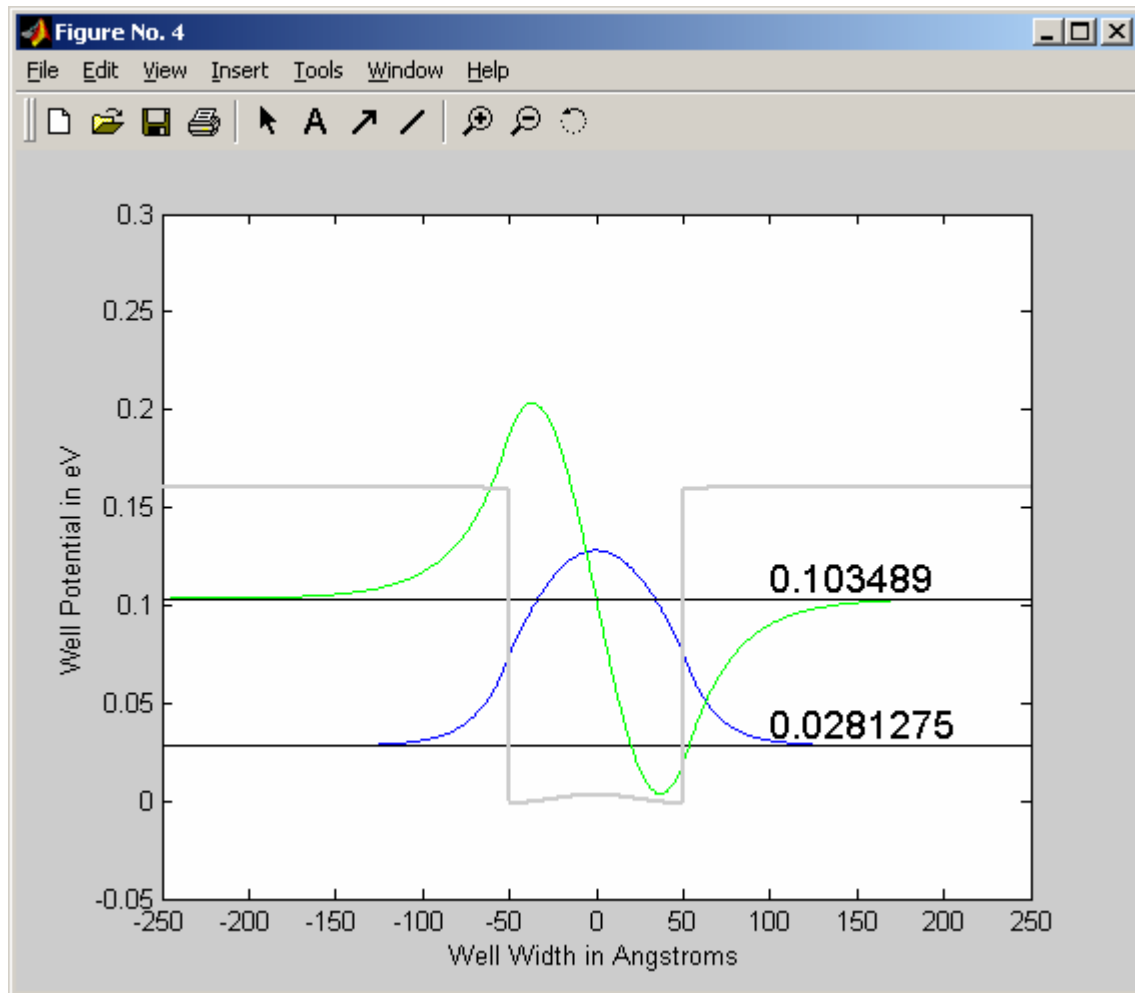


Figure 3.17 Output Screen 3- Self consistent solutions for Example 2 (Energy levels and Wave functions)

## CHAPTER 4

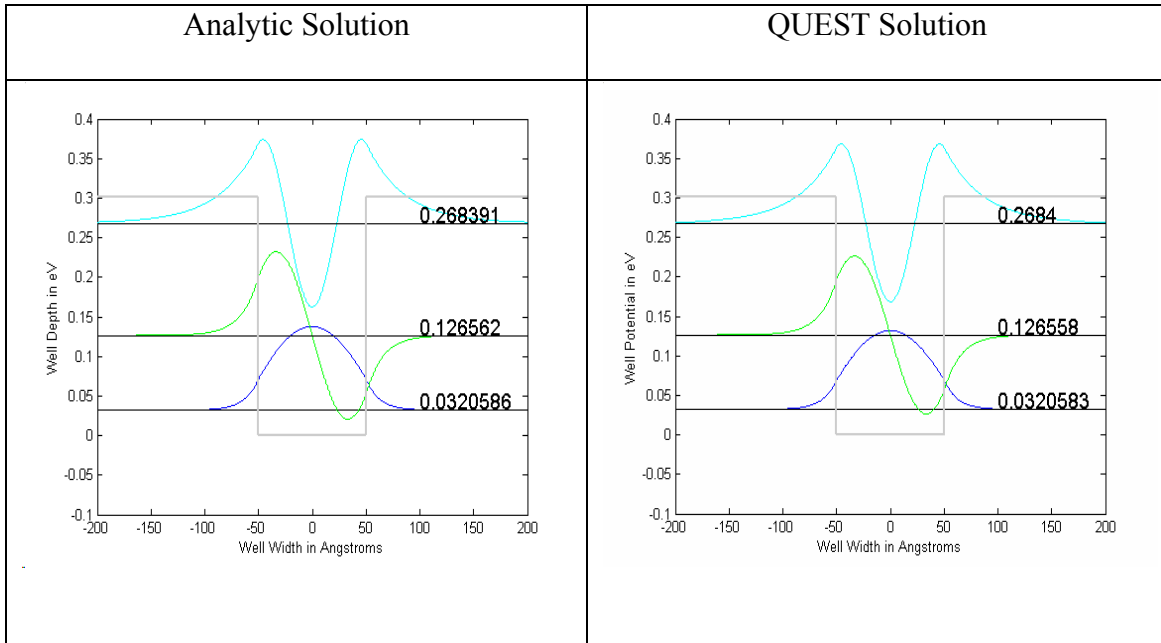
### SIMULATION RESULTS

This chapter contains the simulations and results for different well structures. Results are compared to either analytic solutions or previously published data to verify the validity of the results obtained by QUEST.

#### 4.1 Undoped Rectangular Well

The simulation was carried out by QUEST and a program written in Matlab to calculate the analytic solution for an undoped finite rectangular quantum well with Barrier width =  $150 \text{ \AA}$ ,  $L_w = 100 \text{ \AA}$ ,  $m_w = 0.067$ ,  $m_b = 0.0919$ ,  $V_0 = 0.302 \text{ eV}$ .

Table 4.1 The wave functions and the solutions of a finite rectangular quantum well where the Barrier width =  $150 \text{ \AA}$ ,  $L_w = 100 \text{ \AA}$ ,  $m_w = 0.067$ ,  $m_b = 0.0919$ ,  $V_0 = 0.302 \text{ eV}$ .



The left panel in Table 4.1 shows the analytic solution for the well structure described. The QUEST solution is presented in the right panel for comparison. It can be observed that the solutions/ Eigen values are exact to at least the fourth decimal place and the wave functions have similar shapes. The changes observed in the amplitudes are a matter of different normalizations used and do not reflect on the discrepancies between the two solutions. The solutions/ Eigen values are shown in Table 4.2 for easy comparison of the results generated by each method namely the analytic solution and the numerical/QUEST solutions. Note that the values presented in for Table 4.2 the QUEST solution are obtained from the stored text file which is at a higher precision

(more decimal places) than shown in the graph for the same. This disparity is due to space limitations on a Matlab figure which causes the program to truncate the number.

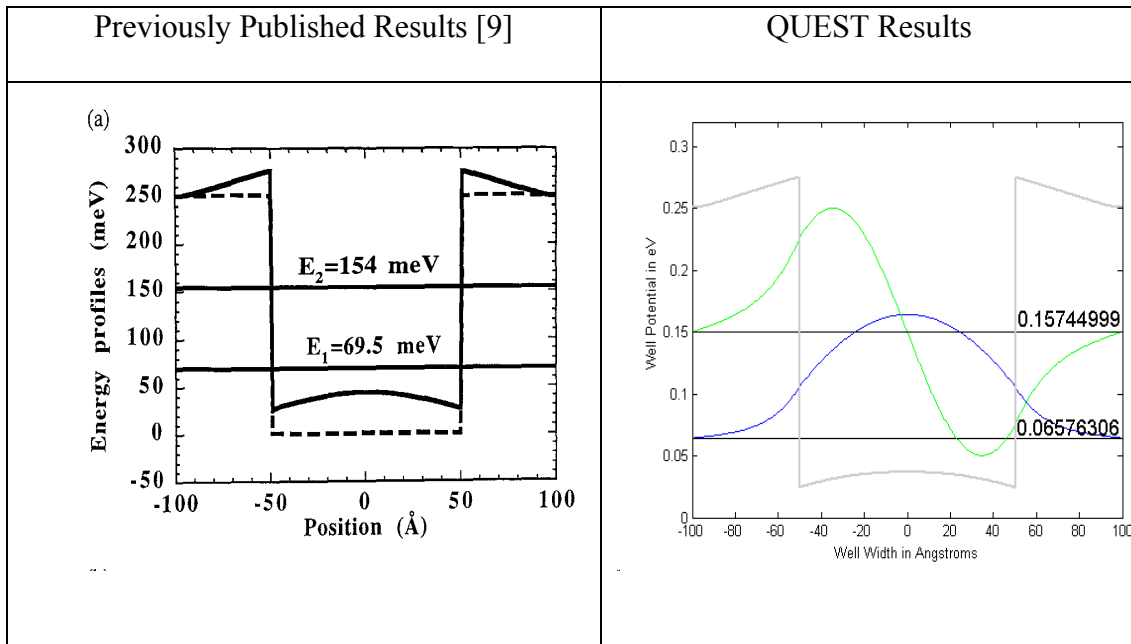
Table 4.2 Solutions of a finite rectangular quantum well where the Barrier width = 150 Å,  $L_w = 100$  Å,  $m_w = 0.067$ ,  $m_b = 0.0919$ ,  $V_0 = 0.302$  eV.

Mode Number	Analytic Solution	QUEST Solution
1	0.0320586	0.032058343
2	0.126562	0.126558409
3	0.268391	0.268400015

#### 4.2 Doped Rectangular Well

The simulation was carried out for a Self consistent potential profile for a GaAs/Al<sub>0.3</sub>Ga<sub>0.7</sub>As quantum well with modulation doping within 10 Å at both ends of the profile  $-100 \text{ Å} \leq x \leq -90 \text{ Å}$  and  $90 \text{ Å} \leq x \leq 100 \text{ Å}$ . The well structure is an n-type modulation doped quantum well and  $N_D = 4E18 \text{ cm}^{-3}$ .

Table 4.3 The wave functions and the solutions of a finite rectangular quantum well where the Barrier width = 50 Å,  $L_w = 100$  Å,  $m_w = 0.067$ ,  $m_b = 0.0919$ ,  $V_0 = 0.251$  eV with modulation doping within 10 Å at both ends of the profile  $-100$  Å  $\leq x \leq -90$  Å and  $90$  Å  $\leq x \leq 100$  Å,  $N_D = 4E18$  cm<sup>-3</sup> [9]



The left panel in Table 4.3 shows the solution from *Physics of Optoelectronic Devices* for the well structure described. The QUEST solution is presented in the right panel for comparison. It can be observed that the solutions/ Eigen values are in agreement within a 5% difference in solutions and the wave functions have similar shapes. The changes observed in the amplitudes are a matter of different normalizations used and do not reflect on the discrepancies between the two solutions. The solutions/ Eigen values are shown in Table 4.4 for easy comparison of the results generated by each method namely the published results and the numerical/QUEST solutions.



Table 4.4 Solutions of a finite rectangular quantum well where the Barrier width = 50 Å,  $L_w = 100$  Å,  $m_w = 0.067$ ,  $m_b = 0.0919$ ,  $V_0 = 0.251$  eV with modulation doping within 10 Å at both ends of the profile  $-100 \text{ Å} \leq x \leq -90 \text{ Å}$  and  $90 \text{ Å} \leq x \leq 100 \text{ Å}$ ,  $N_D = 4E18 \text{ cm}^{-3}$ [9]

Mode Number	Published Results	QUEST Solution
1	0.0695	0.065763060063
2	0.154	0.157449993483

### 4.3 Effects of Electric Field

The potential energy is simply added to the potential term within the appropriate shooting equation i.e

$$V(z) \rightarrow V(z) + qF(z - z_0) \quad (71)$$

where for an electron  $q = -e$  and  $F$  is the electric field. The position  $z_0$  represents the origin of the electric field often chosen to be the center of the well [10].

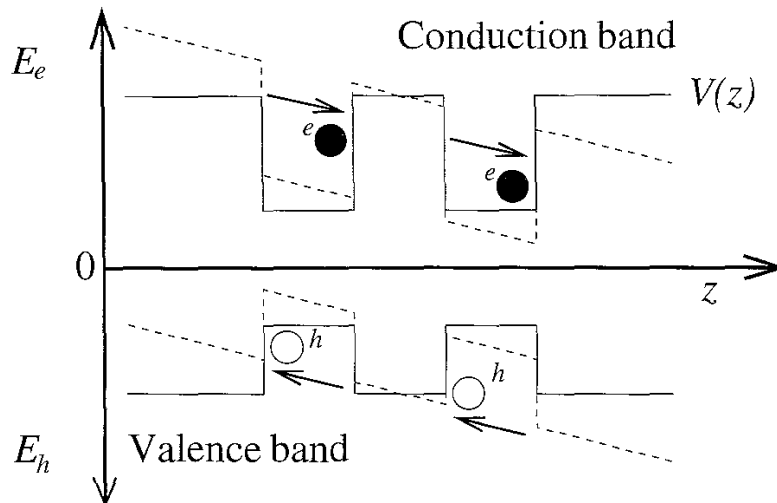


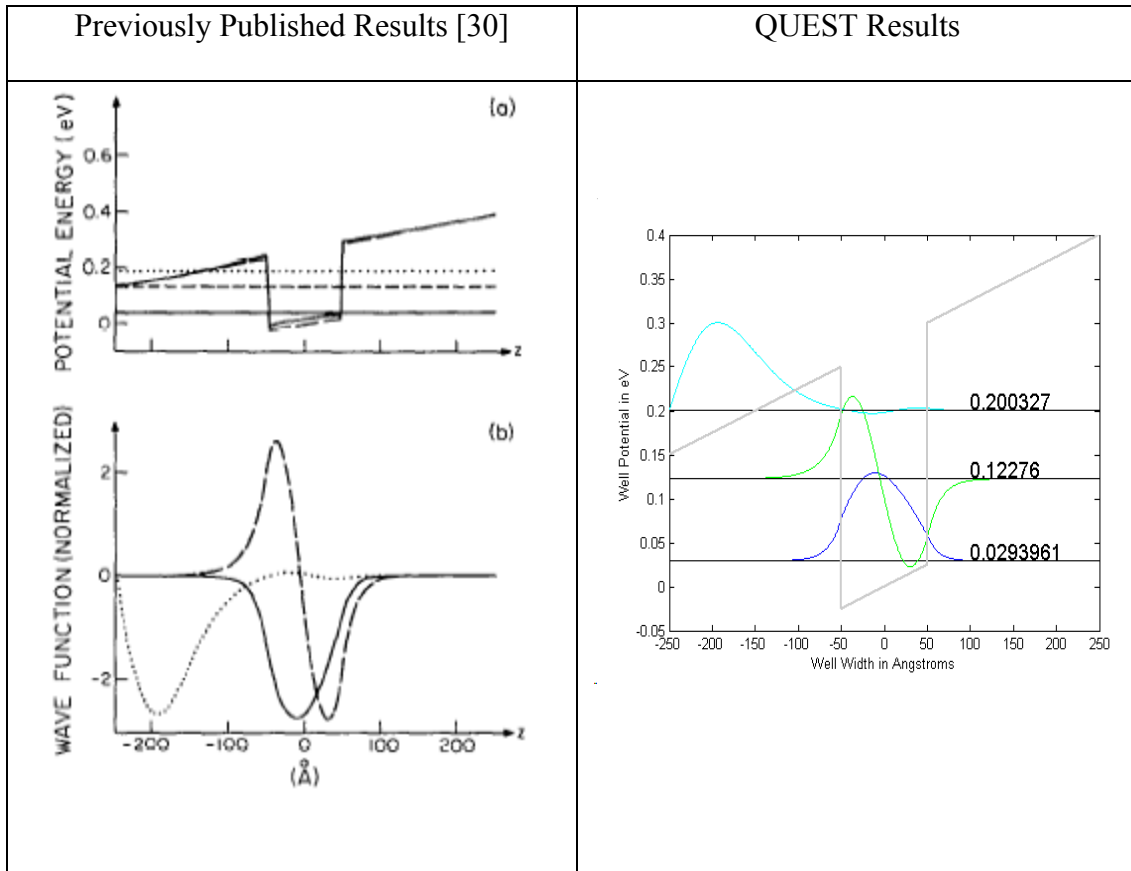
Figure 4.1 Schematic of the tilting of conduction and valence band under the influence of an electric field [10]

Figure 4.1 shows the effect of an electric field on the conduction band potentials; note that the electrons in the double well are pulled to the right side. The amplitude of the wave function within the well decreases when external electric field is applied [28]. This electric field causes electrons at the higher energy levels to tunnel. As field strength is increased, the tunneling phenomenon becomes more pronounced. This effect creates the phenomena known as quantum confined stark effect (QCSE) [29]. The quantum confined stark effect arises when an electric field is applied perpendicular to the plane of the quantum well, inducing polarization of electrons and/or holes, which alters the confined energy states and shifts the absorption resonance to lower energy thus providing the basis for optical modulators and switches. Many modern optoelectronic devices such as high speed modulators and bistable devices are based on the Quantum Confined Stark Effect [10].

#### *4.3.1 Rectangular Well with Applied Electric Field*

The simulation was carried out for a GaAs/Al<sub>0.35</sub>Ga<sub>0.65</sub>As quantum well with finite rectangular quantum well where the Barrier width = 200 Å, well width of  $L_w = 100$  Å, and well mass of  $m_w = 0.0665$ , barrier mass of  $m_b = 0.0957$ , barrier height of  $V_0 = 0.262$  eV, applied electric field  $E = 50$  kV/cm.

Table 4.5 The wave functions and the solutions of a finite rectangular quantum well where the Barrier width = 200 Å,  $L_w = 100$  Å,  $m_w = 0.0665$ ,  $m_b = 0.0957$ ,  $V_0 = 0.262$  eV, Applied electric field  $E = 50$  kV/cm [30]



The left panel in Table 4.5 shows the solution from Roan et al. for the well structure described [30]. The QUEST solution is presented in the right panel for comparison. It can be observed that the solutions/ Eigen values are in agreement and the wave functions have similar shapes. The solutions/ Eigen values are shown in Table 4.6 for comparison of results generated by each method namely the published results and the numerical/QUEST solutions.

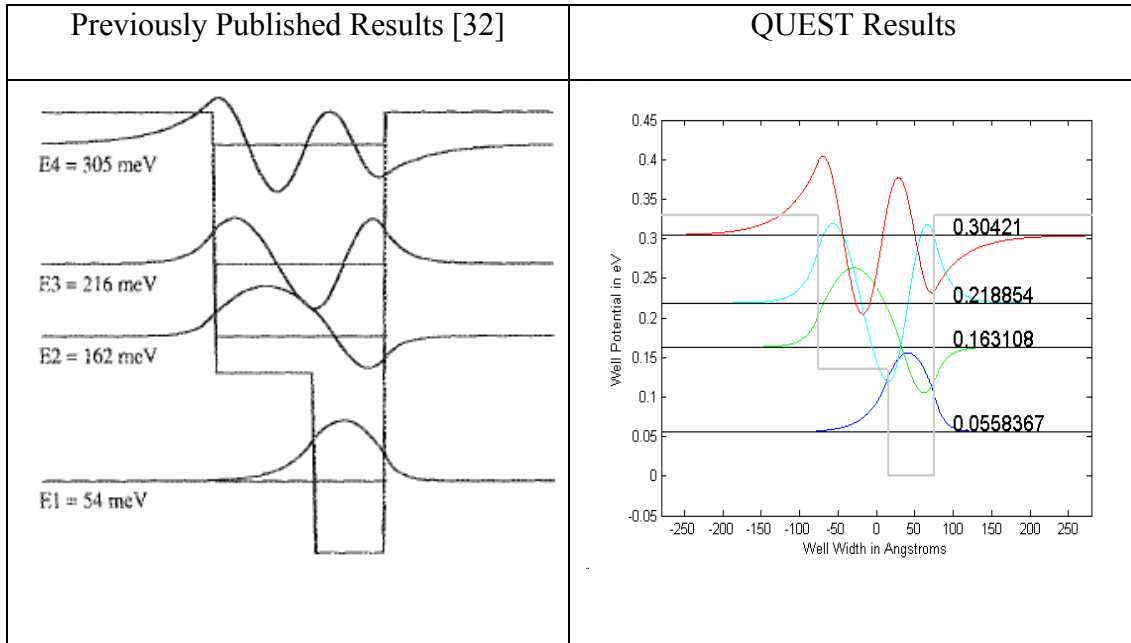
Table 4.6 Solutions of a finite rectangular quantum well where the Barrier width = 200 Å,  $L_w = 100$  Å,  $m_w = 0.0665$ ,  $m_b = 0.0957$ ,  $V_0 = 0.262$  eV, Applied electric field  $E = 50$  kV/cm [30]

Mode Number	Published Results	QUEST Solution
1	0.029	0.029396106572
2	0.125	0.122760024103
3	0.195	0.200327100101

#### 4.4 Asymmetric Well structures: Stepped Well Structures

The efficiency of high speed switching devices can be improved by using asymmetric step quantum wells [31]. An example of such a structure is simulated and the results are presented below. The simulation was carried out for a GaAs quantum well with finite rectangular quantum well where the  $\text{Al}_{0.44}\text{Ga}_{0.56}\text{As}$  barrier of width = 280 Å, well width of  $L_w = 60$  Å with a step of  $\text{Al}_{0.18}\text{Ga}_{0.82}\text{As}$  of width 90 Å, and well mass of  $m_w = 0.0665$ , barrier mass of  $m_b = 0.1$ , step mass of  $m_s = 0.08$  and barrier height of  $V_0 = 0.33$  eV, step height of  $V_s = 0.15$  eV [32]. These structures have been previously used in devices such as high speed optical modulators and optical bistable switches.

Table 4.7 The wave functions and the solutions of a finite rectangular quantum well where the  $\text{Al}_{0.44}\text{Ga}_{0.56}\text{As}$  barrier of width = 280 Å, well width of  $L_w = 60$  Å with a step of  $\text{Al}_{0.18}\text{Ga}_{0.82}\text{As}$  of width 90 Å, and well mass of  $m_w=0.0665$ , barrier mass of  $m_b=0.1$ , step mass of  $m_s=0.08$  and barrier height of  $V_0=0.33$  eV, step height  $V_s=0.15$  eV [32].



The left panel in Table 4.7 shows the solution from Mii et al for the well structure described. The QUEST solution is presented in the right panel for comparison. It can be observed that the solutions/ Eigen values are in agreement and the wave functions have similar shapes. The solutions/ Eigen values are shown in Table 4.8 for comparison of results generated by each method namely the published results and the numerical/QUEST solutions.

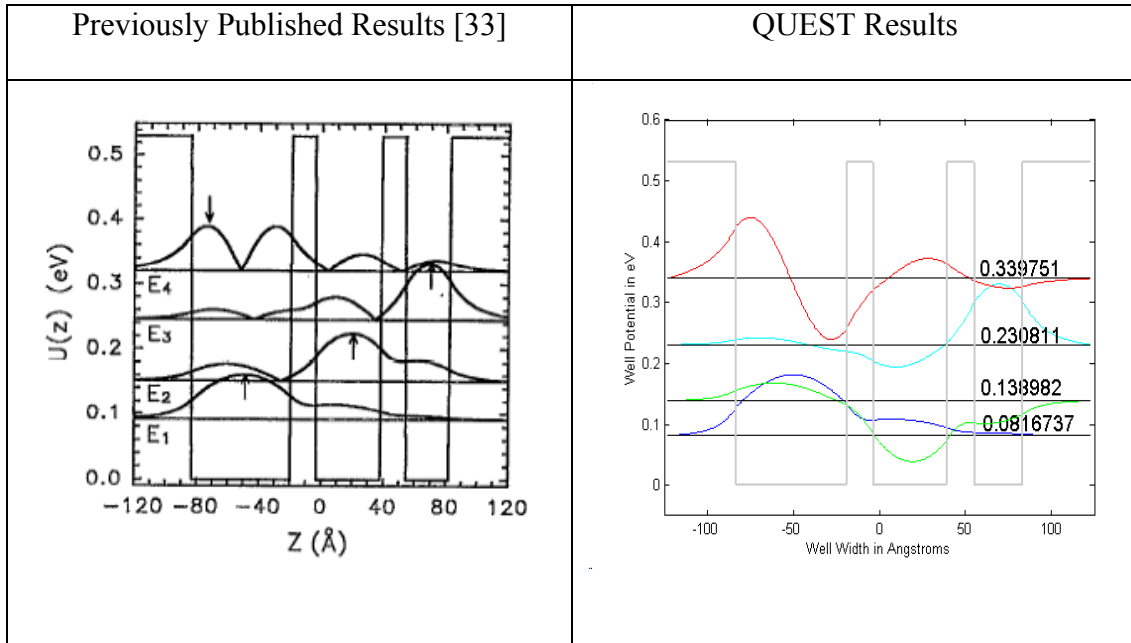
Table 4.8 Solutions of a finite rectangular quantum well where the  $\text{Al}_{0.44}\text{Ga}_{0.56}\text{As}$  barrier of width = 280 Å, well width of  $L_w = 60$  Å with a step of  $\text{Al}_{0.18}\text{Ga}_{0.82}\text{As}$  of width 90 Å , and well mass of  $m_w=0.0665$ , barrier mass of  $m_b=0.1$ , step mass of  $m_s=0.08$  and barrier height of  $V_0=0.33$  eV, step height  $V_s=0.15$  eV [32].

Mode Number	Published Results	QUEST Solution
1	0.054	0.055836702413
2	0.162	0.163108018453
3	0.216	0.218854107531
4	0.305	0.304214359752

#### 4.5 Triple Well Structures

In this section, a three coupled well structure is simulated. The simulation was carried out for an undoped asymmetric triple coupled quantum well structure with three  $\text{Ga}_{0.47}\text{In}_{0.53}\text{As}$  quantum wells with well width of  $L_w = 64$  Å, 42 Å and 28 Å respectively separated by  $\text{Al}_{0.48}\text{In}_{0.52}\text{As}$  barrier of width = 16 Å, and well mass of  $m_w = 0.04$  , barrier mass of  $m_b=0.075$  and barrier height of  $V_0=0.53$  eV [33].

Table 4.9 The wave functions and the solutions of a quantum well structure with three  $\text{Ga}_{0.47}\text{In}_{0.53}\text{As}$  quantum wells with well width of  $L_w = 64 \text{ \AA}$ ,  $42 \text{ \AA}$  and  $28 \text{ \AA}$  respectively separated by  $\text{Al}_{0.48}\text{In}_{0.52}\text{As}$  barrier of width =  $16 \text{ \AA}$ , and well mass of  $m_w = 0.04$ , barrier mass of  $m_b = 0.075$  and barrier height of  $V_0 = 0.53 \text{ eV}$  [33]



The left panel in Table 4.9 shows the solution from Huang et al. for the well structure described [33]. The QUEST solution is presented in the right panel for comparison. It can be observed that the solutions/ Eigen values are comparable and the wave functions have similar shapes. The solutions/ Eigen values are shown in Table 4.10 for comparison of results generated by each method namely the published results and the numerical/QUEST solutions.

Table 4.10 Solutions of a quantum well structure with three  $\text{Ga}_{0.47}\text{In}_{0.53}\text{As}$  quantum wells with well width of  $L_w = 64 \text{ \AA}$ ,  $42 \text{ \AA}$  and  $28 \text{ \AA}$  respectively, separated by  $\text{Al}_{0.48}\text{In}_{0.52}\text{As}$  barrier of width =  $16 \text{ \AA}$ , and well mass of  $m_w = 0.04$ , barrier mass of  $m_b = 0.075$  and barrier height of  $V_0 = 0.53 \text{ eV}$  [33].

Mode Number	Published Results	QUEST Solution
1	0.085	0.081673715241
2	0.135	0.138982437801
3	0.240	0.230811011403
4	0.325	0.339751645232

#### 4.6 Chirped Well Structure

This section contains simulations for a chirped quantum well structure with two different applied electric fields. The well configurations are about  $100 \text{ \AA}$  wide and are bound by AlAs barriers. The chirped well is divided into six sections that are 6 monolayers thick. The sections are composed of the following configuration: Number of GaAs monolayers=(y), Number of  $\text{Al}_{0.2}\text{Ga}_{0.8}\text{As}$  monolayers = (6-y) where a monolayer width equals  $2.83 \text{ \AA}$ . For example, for the first section  $y = 6$  that is the sections consists of 6 monolayers of GaAs and 0 monolayers of  $\text{Al}_{0.2}\text{Ga}_{0.8}\text{As}$ . Consecutive sections are composed of  $y = 5, 4, 3, 2$  and 1 of the described composition of GaAs/ $\text{Al}_{0.2}\text{Ga}_{0.8}\text{As}$ . The barriers that bind the well were simulated with a height of  $0.44 \text{ eV}$  while the heights for the barriers that separate each chirped section of the well were set at  $0.149 \text{ eV}$ . The simulation assumed a well mass of  $m_w = 0.04$ , binding barrier mass of  $m_b = 0.15$  and separating barrier mass of  $m_b = 0.08$  respectively [34].

The left panel in Table 4.11 shows the solution for the well structure described. The QUEST solution is presented in the right panel for comparison. The same well



structure described above is simulated with an applied electric field of  $E = 128.571$  kV/cm and  $E = 257.143$  kV/cm and the results are presented in Table 4.12 and Table 4.13 respectively. It can be observed that the solutions/ Eigen values are comparable and the wave functions have similar shapes. The solutions/ Eigen values are shown in Table 4.14 for comparison of results generated by each method.

Table 4.11 The wave functions and the solutions of a chirped rectangular quantum well where the Barrier width =  $150 \text{ \AA}$ ,  $L_w \sim 100 \text{ \AA}$  (36 monolayers),  $m_w = 0.067$ ,  $m_b = 0.15$ ,  $V_0 = 0.044 \text{ eV}$  [34]

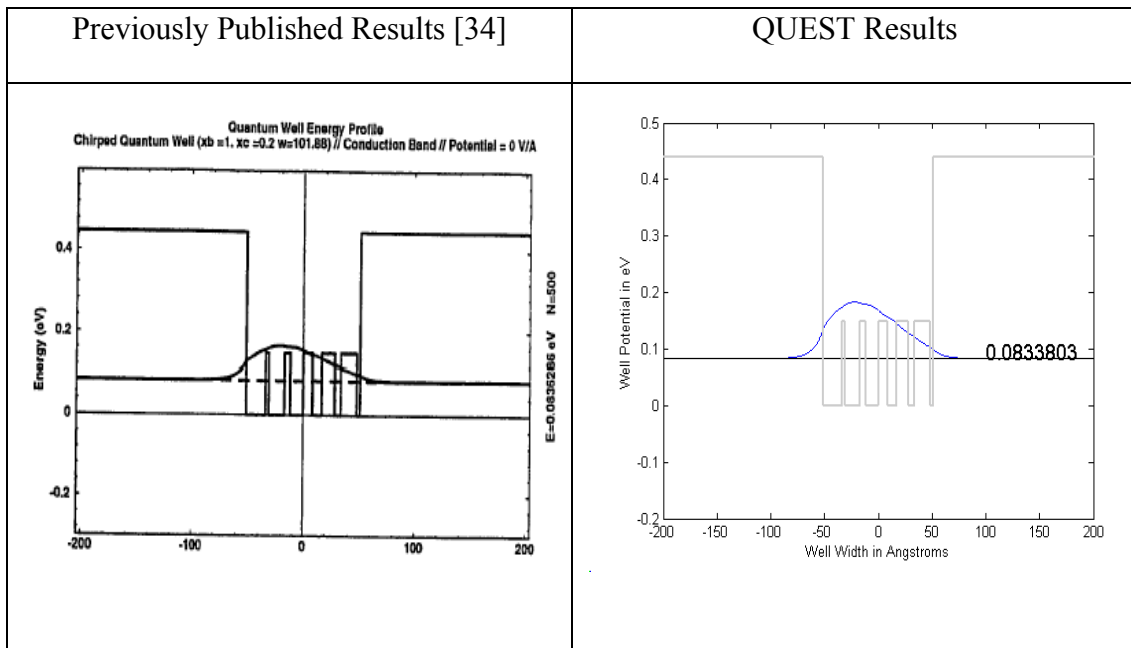


Table 4.12 The wave functions and the solutions of a chirped rectangular quantum well where the Barrier width =  $150 \text{ \AA}$ ,  $L_w \sim 100 \text{ \AA}$  (36 monolayers),  $m_w = 0.067$ ,  $m_b = 0.15$ ,  $V_0 = 0.044 \text{ eV}$ , Applied electric field  $E = 128.571 \text{ kV/cm}$  [34]

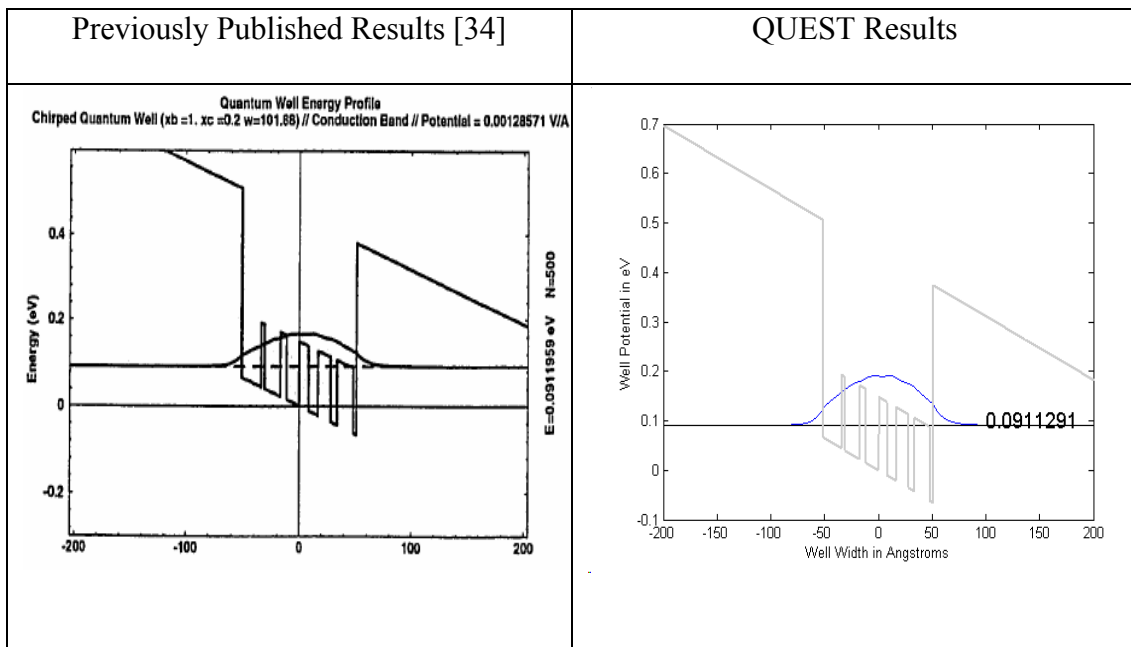


Table 4.13 The wave functions and the solutions of a chirped rectangular quantum well where the Barrier width =  $150 \text{ \AA}$ ,  $L_w \sim 100 \text{ \AA}$  (36 monolayers),  $m_w = 0.067$ ,  $m_b = 0.15$ ,  $V_0 = 0.044 \text{ eV}$ , Applied electric field  $E = 257.143 \text{ kV/cm}$  [34]

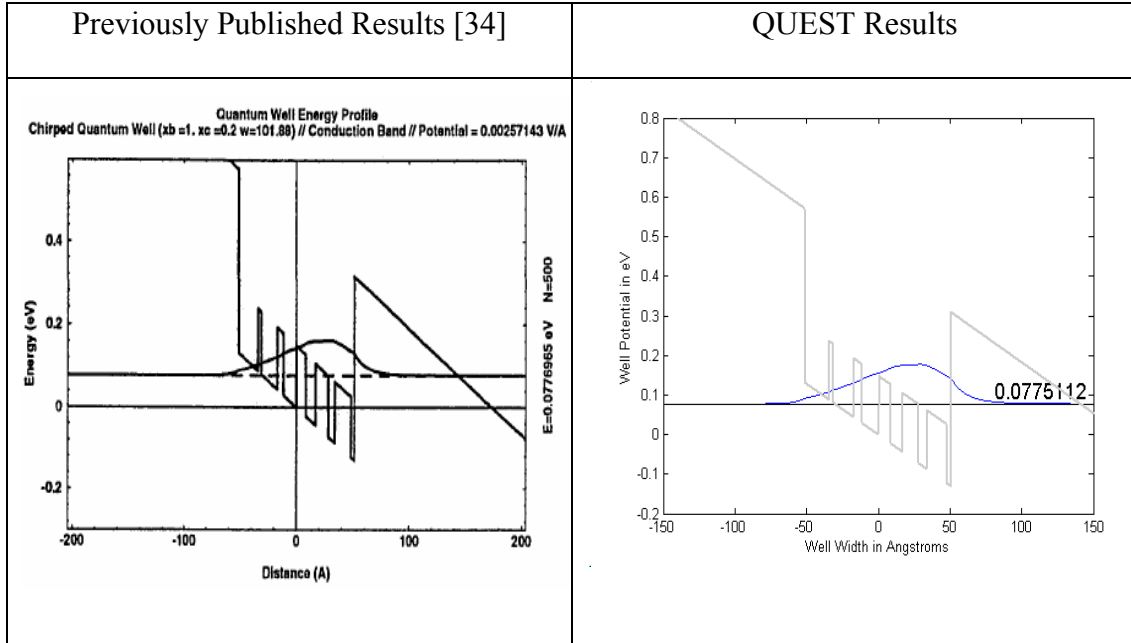


Table 4.14 Solutions of a quantum well structure where the Barrier width =  $150 \text{ \AA}$ ,  $L_w \sim 100 \text{ \AA}$  (36 monolayers),  $m_w = 0.067$ ,  $m_b = 0.15$ ,  $V_0 = 0.044 \text{ eV}$  [34]

Applied field (kV/cm)	Mode Number	Published Results	QUEST Solution
0	1	0.0836286	0.083380365310
128.571	1	0.0911959	0.091129186957
257.143	1	0.0776968	0.077511226538

## CHAPTER 5

### DEVICE APPLICATION

The past several years have seen tremendous growth in the research and development of devices based on quantum well intersubband transitions in very useful and varied applications [35,36]. The interest was heightened by the simultaneous improvements in III-V semiconductor technology and by new semiconductor growth methods. GaAs semiconductor technology provides several advantages such as relatively low cost, high yield, and the flexibility in band tailoring to function under a wide range of operating conditions [37].

#### 5.1 Quantum Well Infrared Photodetector

The device explored in this chapter as a possible application is the Quantum Well Infrared Photodetectors (QWIPs). One significant benefit of using QWIPs is the ability to operate in two disparate wavelength windows by proper tailoring of the device design using band gap engineering that can be tested at the simulation level [3, 38]. This is also the reason why this device is presented as an application of QUEST to emphasize the relevance of such a simulation tool prior to fabrication in the laboratory. A detector that is accurately tuned to desired wavelengths can be used in applications such as on a military aircraft as a laser spot tracker or an infrared camera with good precision and dependability [4].

## 5.2 Application of Electric Field

The effect of an electric field on electronic subbands called the quantum confined Stark effect is used in conjunction with the aforementioned properties in semiconductor quantum well structures to modify the fundamental physical properties for applications in optoelectronic and communication devices [39-41]. Coupling between double quantum wells separated by a narrow barrier can dramatically enhance the energy shift induced by the electric field. This property has been previously exploited in the fabrication of electro-optical devices such as modulators and switches.  $\text{In}_x\text{Ga}_{1-x}\text{As} / \text{In}_y\text{Al}_{1-y}\text{As}$  quantum well structures have a larger conduction-band as compared to  $\text{Al}_x\text{Ga}_{1-x}\text{As}/\text{GaAs}$  structures and are hence used in the QUEST simulation to aid band gap engineering for the proposed far-infrared detector operating in the atmospheric window spectral region between 10 and 20  $\mu\text{m}$  [42]. While the device proposed in this section is a voltage tunable QWIP, these materials are also very attractive due to their potential applications in high-speed electronic and long-wavelength devices due to their large conduction and discontinuity and the existence of several subbands in the quantum wells [40]. The operation of a QWIP is based on the absorption by electrons in the infrared region by the intersubband transitions of the first five subbands that exist in the  $\text{In}_x\text{Ga}_{1-x}\text{As} / \text{In}_y\text{Al}_{1-y}\text{As}$  coupled quantum wells as demonstrated in Table 5.1.

## 5.3 Calculation of Absorption

A separate program was used to calculate and plot the absorption in a given well structure. The wavefunctions and the states that were generated using QUEST serve as

inputs to this program module. This program module will be integrated into QUEST in the future. The absorption that is calculated is considered to primarily result from the intersubband transitions of the doped quantum well structure [43]. The program is based on the assumption that the doping is not very large and thus screening effects due to electron to electron coulomb interaction are negligible [44].

### 5.3.1 Calculation of Absorption Spectrum

Consider two states with energies,  $E_a$  and  $E_b$ , respectively (in the simulation  $a=2$  and  $b=3$  that is the  $E_3 \rightarrow E_2$  intersubband transition is demonstrated). The nonzero absorption coefficient that results from the intersubband transitions from  $E_b$  to  $E_a$  is calculated for  $\hat{e} = \hat{x}$  that is TM polarization and the  $y$  and  $z$  components of the intersubband dipole moment are zero. The absorption coefficient is given by Equation 72 [9, 45, 46].

$$\alpha(\hbar\omega) = \left( \frac{\omega}{n_r c \varepsilon_0} \right) \frac{|\mu_{ba}|^2 (\Gamma/2)}{(E_b - E_a - \hbar\omega)^2 + (\Gamma/2)^2} (N_a - N_b) \quad (72)$$

where the intersubband dipole moment  $\mu_{ba}$  is given by Equation 73 [9]

$$\mu_{ba} = \langle \Psi_b | ex | \Psi_a \rangle = \int \Psi_b^*(x) ex \Psi_a(x) dx \quad (73)$$

and  $N_i$  is the number of electrons per unit volume in the  $i^{\text{th}}$  subband (Equation 74) [9].

$$N_i = \frac{m_e^* k_B T}{\pi \hbar^2 L_x} \ln(1 + e^{(E_F - E_i)/(k_B T)}) \quad (74)$$

## 5.4 Simulated Structure Parameters

The sample structures simulated in this section uses an  $\text{In}_{0.65}\text{Ga}_{0.35}\text{As}$  /  $\text{In}_{0.52}\text{Al}_{0.48}\text{As}$  coupled double quantum well material system. The structure consists of

two  $\text{In}_{0.65}\text{Ga}_{0.35}\text{As}$  wells and  $\text{In}_{0.52}\text{Al}_{0.48}\text{As}$  barriers. The thicknesses of the left and right  $\text{In}_{0.65}\text{Ga}_{0.35}\text{As}$  wells was set to be  $50\text{Å}$  and  $100\text{Å}$  respectively, while the  $\text{In}_{0.52}\text{Al}_{0.48}\text{As}$  center barrier width was set at  $30\text{Å}$  with binding/surrounding barrier widths of  $150\text{Å}$ . The subband energies and the energy wave functions were calculated using the simulation tool QUEST. The dielectric constant of  $\text{In}_{0.65}\text{Ga}_{0.35}\text{As}$  was taken to be 13.5. The electron effective mass values of the  $\text{In}_{0.52}\text{Al}_{0.48}\text{As}$  barrier and the  $\text{In}_{0.65}\text{Ga}_{0.35}\text{As}$  well were set at 0.13663 and  $0.03654 m_0$ , respectively [40].

Table 16 shows the wavefunctions, states and absorption spectra ( $E_3 \rightarrow E_2$  intersubband transition) for the simulated well structure. It is observed that the wavelength at which the absorption peaks, changes with an applied electric field demonstrating QCSE, which is the basic working principle of voltage tunable photodetectors/QWIPs. When there is no applied electric field,  $E=0\text{ kV/cm}$ , the wavelength at which maximum absorption occurs is  $\lambda_{max} \approx 19.25\text{ }\mu\text{m}$ . However when electric field,  $E=-50\text{ kV/cm}$ , the wavelength at which maximum absorption occurs is  $\lambda_{max} \approx 10.55\text{ }\mu\text{m}$  and when electric field,  $E=50\text{ kV/cm}$ , the wavelength at which maximum absorption occurs is  $\lambda_{max} \approx 95\text{ }\mu\text{m}$  [40].

To summarize the results, a wavelength shift of  $\Delta\lambda \approx 8.7\text{ }\mu\text{m}$  is observed when an electric field of  $E=-50\text{ kV/cm}$ , is applied to the well structure. The operating range of the electric field for this device is  $-50 \leq E \leq 0\text{ kV/cm}$ . The example of applied electric field,  $E=50\text{ kV/cm}$ , is simulated to explore the characteristics of the well structure and demonstrate the QCSE and not necessarily for device operation [40]. In the case of a negative applied electric field (used in device operation), the wavefunctions move to the

left and the magnitude of the energy states increases that is the application of an applied field shifts the intersubband energy and increases the absorption at the operating wavelength. Quantum well structures can be also designed so that the intersubband absorption occurs at the operating wavelength and decreases with applied field.

The simulated well structure was based on an  $\text{In}_{0.65}\text{Ga}_{0.35}\text{As} / \text{In}_{0.52}\text{Al}_{0.48}\text{As}$  material system and this material system was chosen to provide the desired operating long infrared wavelength range [47]. The results also indicate that the large intersubband Stark effect in  $\text{In}_{0.65}\text{Ga}_{0.35}\text{As} / \text{In}_{0.52}\text{Al}_{0.48}\text{As}$  coupled double quantum wells may be useful for the fabrication optical modulation devices and voltage tunable QWIPs based on the transfer of electrons between coupled quantum wells under an applied bias.



Table 5.1 Plots that show the wavefunctions, states and absorption spectra for the well structure with  $\text{In}_{0.65}\text{Ga}_{0.35}\text{As}$  wells of  $50\text{\AA}$  and  $100\text{\AA}$ ,  $\text{In}_{0.52}\text{Al}_{0.48}\text{As}$  center barrier of  $30\text{\AA}$ , surrounding barrier widths of  $150\text{\AA}$  under applied electric field of  $0, -50$  and  $50$  kV/cm. The effective mass values of the  $\text{In}_{0.52}\text{Al}_{0.48}\text{As}$  barrier and the  $\text{In}_{0.65}\text{Ga}_{0.35}\text{As}$  are  $0.13663 m_0$  and  $0.03654 m_0$  [40].

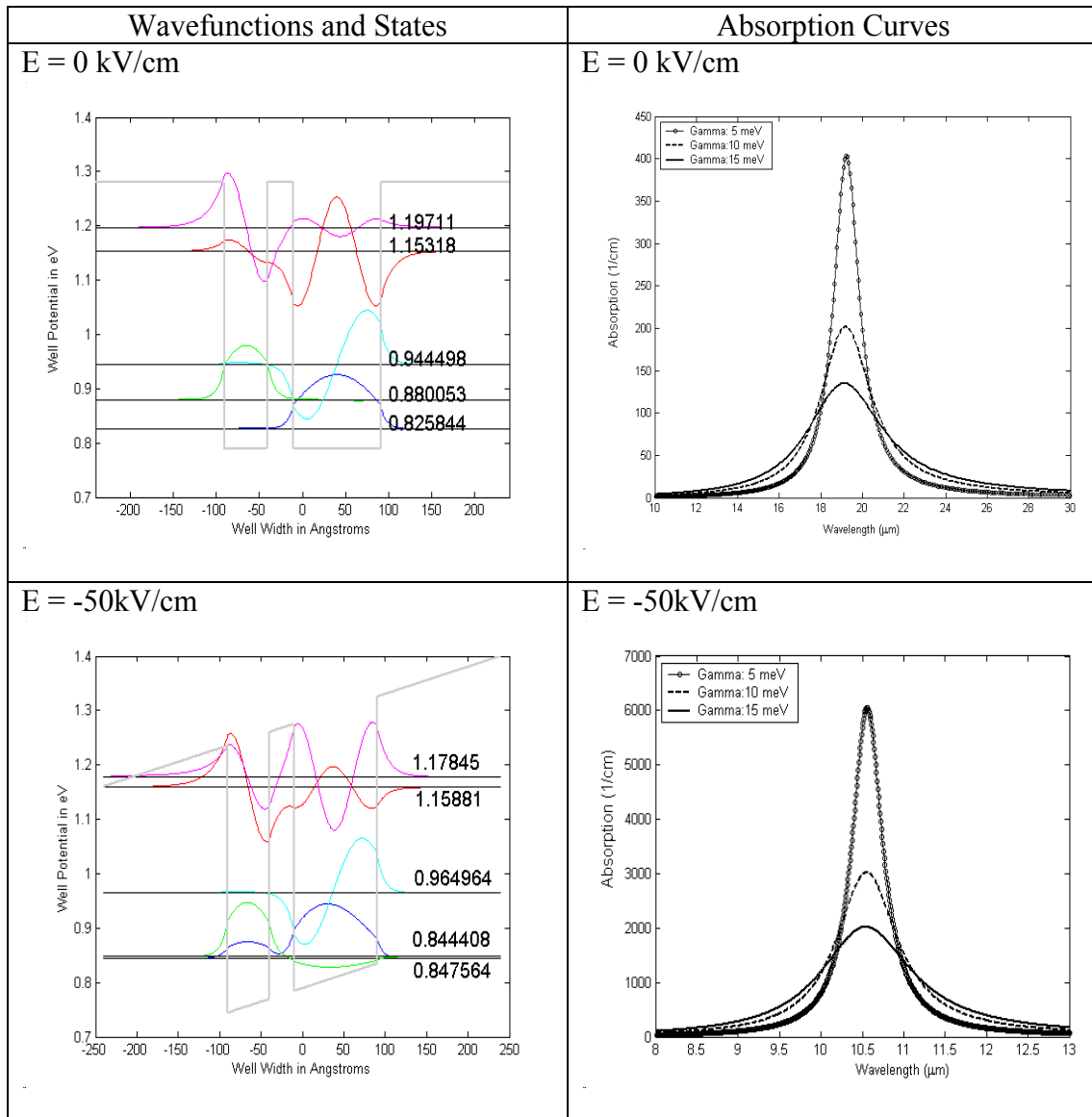
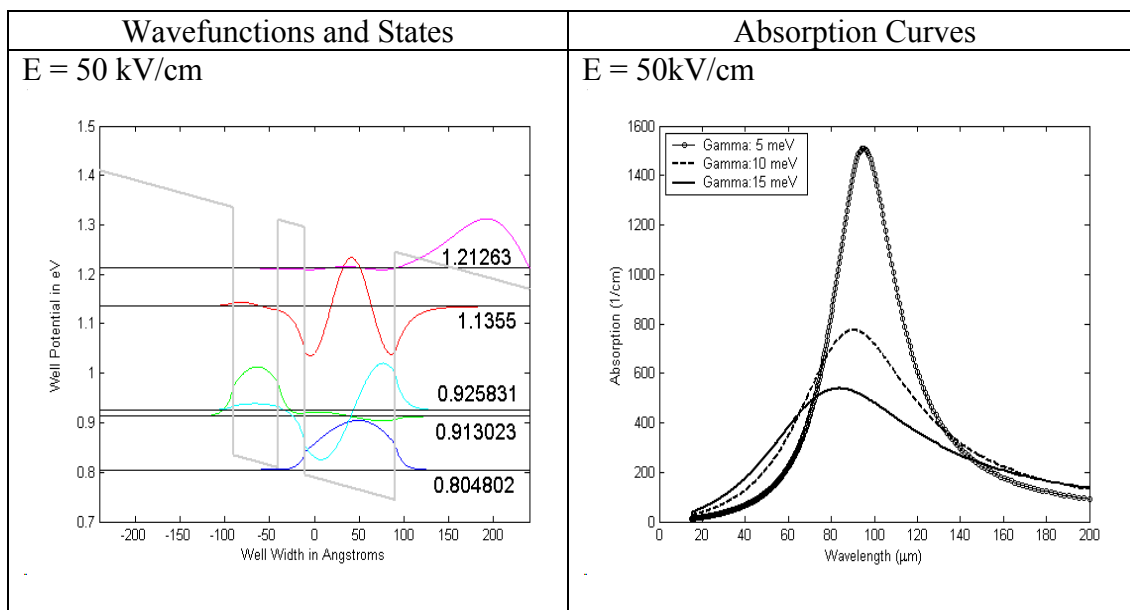


Table 5.1-Continued



## CHAPTER 6

### SUMMARY AND FUTURE WORK

#### 6.1 Specific Achievements

The primary goal of this thesis was to build an integrated simulation tool suite to solve for energy levels and wavefunctions for the conduction band of arbitrary shaped well structures. The thesis focuses on simulation of these user input well structures to model their behavior for application to devices based on intersubband transitions.

Pursuant to this goal the thesis provides simulations of varied quantum well systems that are compared to previously published results to establish their validity and accuracy. Specifically the thesis makes the following contributions.

1. Provides an integrated tool suite (QUEST) built in Matlab that can perform calculations for bandgap engineering and material optimization
2. This tool suite is unique in that all key elements that required designing a device and tailoring its characteristics using bandgap engineering are integrated into a single user friendly program with a GUI.
3. Advanced features such as effects of externally applied electric field, doping and absorption curves are also explored.
4. A comprehensive user manual is provided to guide a new user through the process of simulation.

5. QUEST simulations of several quantum well structures are presented with previously published results to validate the results and compare the degree of accuracy for QUEST predictions.
6. Finally a device design of a quantum well infrared photodetector (QWIP) is discussed and the operational characteristics are related to the optimized design using QUEST.

## 6.2 Future Work

Future work can be categorized into two distinct directions: first, development of the simulation capabilities of QUEST to include additional features for material optimization and device design; and second, the software capabilities of QUEST which include enhancing the user interface and refinement of the software suite.

Simulation Capabilities that will be added in the future include addition of calculations for valence band energy states and wave functions. This will enable the user to simulate the behavior caused by exciton interactions. The absorption program that is currently a separate module will be integrated into the QUEST tool suite.

Software Capabilities that will be worked on will be to improve the graphical user interface (GUI) of the program. These will include the addition of capabilities that will allow the user to enter a potential profile as a function and to enter the material profile from a preexisting file. This will streamline the operation of the program which is important while entering complex well structures.

## REFERENCES

- [1] Y. Segawa, H. Tashiro, and B.-p.Zhang, "<http://www.phys.tohoku.ac.jp/shoukai>" Laser Quantum Optics Group, 2005.
- [2] J. A. Trezza, "Optimization of quantum well optoelectronic modulators," in *Electrical Engineering*. Stanford: Stanford University, 1995, pp. 131.
- [3] B. F. Levine, "Quantum well infrared photodetectors," *Journal of applied physics*, vol. 74, pp. R1-R81, 1993.
- [4] P. Bhattacharya, *Properties of III-V quantum wells and superlattices*. London: INSPEC, The Institution of Electrical Engineers, 1996.
- [5] S. M.-J. Okhovat-Alavian, A. Afzali-Kusha, and M. Kamarei, "Intersubband transitions in different structures of conduction-band quantum wells," presented at The 12<sup>th</sup> International Conference on Microelectronics, Tehran, 2000.
- [6] B. F. Levine, "Device Physics of quantum well infrared photodetectors," *Semiconductor Science Technology*, vol. 8, pp. S400-S405, 1993.
- [7] V. Krishnamurthy, "Design and modeling of asymmetric Fabry Perot Electroreflection modulator," in *Electrical Engineering*. Arlington: The University of Texas at Arlington, 2004, pp. 118.
- [8] B. V. Zeghbroeck, *Principles of Semiconductor Devices*. Boulder, 2004.
- [9] S. L. Chuang, *Physics of Optoelectronic Devices*, First ed. New York: John Wiley and sons, 1995.
- [10] P. Harrison, *Quantum Wells, Wires and Dots: Theoretical and Computational Physics*, First ed. West Sussex: John Wiley and sons, 2001.
- [11] R. F. Pierret, *Advanced semiconductor fundamentals*, vol. VI, Second ed. New Jersey: Prentice Hall, 2003.
- [12] "<http://britneyspears.ac/physics/fbarr/fbarr.html>," 2005.

- [13] A. Witkin and D. Baraff, "An Introduction to Physically Based Modeling: Differential Equation Basics," School of Computer Science, Carnegie Mellon University 1997.
- [14] L. F. Shampine and M. W. Reichelt, "The MATLAB ODE Suite," *SIAM Journal of Scientific Computing*, vol. 18, pp. 1-22, 1997.
- [15] W. H. Press, S. A. Teukolsky, W. T. Vetterling, and B. P. Flannery, *Numerical Recipes in C: The Art of Scientific Computing*, Second ed. New York: Cambridge University Press, 1992.
- [16] J. R. Dormand and P. J. Prince, "High Order Embedded Runge-Kutta Formulae," *Journal of Computational and Applied Mathematics*, vol. 7, pp. 203-211, 1981.
- [17] Mathworks, "MATLAB® The Language of Technical Computing," 2: F-O ed. Natick, MA: The Mathworks, 2004.
- [18] D. Houcque, "Applications of MATLAB: Ordinary Differential Equations (ODE)," Robert R. McCormick School of Engineering and Applied Science - Northwestern University, Evanston.
- [19] J. R. Dormand and P. J. Prince, "A Family of Imbedded Runge-Kutta Formulae," *Journal of Computational and Applied Mathematics*, vol. 6, pp. 19-27, 1980.
- [20] J. R. Dormand, *Numerical Methods for Differential Equations*: CRC Press, 1996.
- [21] G. Grabner, R. Kittinger, and A. Kecskeméthy, "An Integrated Runge-Kutta and polynomial root finding method for reliable event-driven multibody simulation," presented at IFAC Workshop on Lagrangian and Hamiltonian Methods for Nonlinear Control, Seville, 2003.
- [22] T. B. Bahder, *Mathematica for scientists and engineers*, First ed. New York: Addison-Wesley publishing company, 1995.
- [23] B. P. Bailey, M. K. Gordon, and L. F. Shampine, "Automatic solution of the Sturm Liouville problem," *ACM transactions on mathematical software*, vol. 4, 1978.
- [24] H. B. Keller, *Numerical solutions of two point boundary value problem*. City, MA: Blaisdell Publishing company, 1968.

- [25] J. E. Moussa, "The Schrodinger-Poisson selfconsistency in layered quantum semiconductor structures," in *Physics*. Worcester: Worcester Polytechnic Institute, 2003, pp. 37.
- [26] J. L. Educato and J. P. Leburton, "Intersubband relaxation in modulation-doped multiple-quantum-well structures," *Physical Review B*, vol. 49, pp. 2177-2180, 1994.
- [27] A. Blom, "Computer algorithms for solving the Schrodinger and Poisson equations," Division of Solid State Theory, Department of Physics, Lund University, Lund, Sweden December 2, 2002 2002.
- [28] A. Badakhshan, C. Durbin, R. Glosser, K. Alavi, S. Nicholas, D. Dale, and K. Capuder., "Correlation Between Electric Field, Temperature and Carrier Concentration with Respect to Photoreflectance Lineshape at the E1 Transition of GaAs," presented at Materials Research Society Symposium Proceedings-Defect Engineering in Semiconductor Growth, Processing and Device Technology, San Francisco, CA, 1992.
- [29] A. Harwit and J. J.S. Harris, "Observation of Stark shifts in quantum well intersubband transitions," *Applied Physics Letters*, vol. 50, pp. 685-687, 1987.
- [30] E. J. Roan and S. L. Chuang, "Linear and nonlinear intersubband electroabsorptions in a modulation-doped quantum well," *Journal of applied physics*, vol. 69, pp. 3249-3260, 1990.
- [31] C. W. Cheah, G. Karunasiri, and L. S. Tan, "Analysis of AlGaAs/GaAs/InGaAs n-type step multiple quantum wells for the optimization of normal incident absorption," *Semiconductor Science Technology*, vol. 17, pp. 1028-1037, 2002.
- [32] Y. J. Mii, K. L. Wang, R. P. G. Karunasiri, and P. F. Yuh, "Obsevation of large oscillator strengths for both 1->2 and 1->3 intersubband transitions of step quantum wells," *Applied Physics Letters*, vol. 56, pp. 1046-1048, 1990.
- [33] Y. Huang and C. Lien, "Strong Stark effect of the intersubband transitions in the three coupled quantum wells: Application to voltage-tunable midinfrared photodetectors," *Journal of applied physics*, vol. 78, pp. 2700-2706, 1995.
- [34] C. L. Goldsmith, "Design and modeling of multiple quantum well electro-optic intensity modulators," in *Electrical Engineering*. Arlington: The University of Texas at Arlington, 1995, pp. 183.

- [35] B. F. Levine, K. K. Choi, C. G. Bethea, J. Walker, and R. J. Malik, "New 10  $\mu\text{m}$  infrared detector using intersubband absorption in resonant tunnelling GaAlAs superlattices," *Applied Physics Letters*, vol. 50, pp. 1092-1094, 1987.
- [36] R. Kapon, A. Segev, and A. Saar, "Intersubband electro-optic modulators for near and mid infrared applications," *Superlattices and Microstructures*, vol. 23, pp. 1083-1091, 1998.
- [37] A. Guzman, J. L. Sanchez-Rojas, M. G. Tijero, J. Hernando, E. Calleja, E. Munoz, G. Vergara, R. Almazan, F. J. Sanchez, M. Verdu, and M. T. Montojo, "Voltage-tunable two-colour quantum well infrared detector with Al-graded triangular confinement barriers," *Semiconductor Science Technology*, vol. 16, pp. 285-288, 2001.
- [38] J. L. Pan and C. G. F. Jr., "Theory, fabrication and characterization of quantum well infrared photodetectors," *Materials Science and Engineering*, vol. 28, pp. 65-147, 1999.
- [39] A. J. Moseley, D. J. Robbins, A. C. Marshall, M. Q. Kearley, and J. I. Davies, "Quantum confined Stark effect in InGaAs/InP single quantum wells investigated by photocurrent spectroscopy," *Semiconductor Science Technology*, vol. 4, pp. 184-190, 1989.
- [40] T. W. Kim and D. U. Lee, "Enhancement of the intersubband Stark effect in strained  $\text{In}_x\text{Ga}_{1-x}\text{As}/\text{In}_y\text{Al}_{1-y}\text{As}$  asymmetric coupled double quantum wells," *Applied Surface Science*, vol. 153, pp. 96-101, 2000.
- [41] D. A. B. Miller, D. S. Chemla, T. C. Damen, A. C. Gossard, W. Wiegmann, T. H. Wood, and C. A. Burrus, "Bandedge Electro-absorption in Quantum Well Structures: The Quantum Confined Stark Effect," *Physical Review Letters*, vol. 53, pp. 2173-2177, 1984.
- [42] T. W. Kim and J. H. Kim, "Effect of an applied electric field on intersubband transitions in strained  $\text{In}_x\text{Ga}_{1-x}\text{As}/\text{InP}$  coupled double step quantum wells," *Solid State Communications*, vol. 108, pp. 845-849, 1998.
- [43] M. Helm, W. Hilber, T. Fromherz, F. M. Peeters, K. Alavi, and R. N. Pathak, "Infrared absorption in superlattices: A probe of the miniband dispersion and the structure of the impurity band," *Physical Review B*, vol. 48, pp. 1601-1606, 1993.
- [44] M. N. Islam, R. L. Hillman, D. A. B. Miller, D.S.Chemla, A. C. Goddard, and J. H. English, "Electroabsorption in GaAs/AlGaAs coupled quantum well waveguides," *Applied Physics Letters*, vol. 50, pp. 1098-1100, 1986.



- [45] P.-f. Yuh and K. L. Wang, "Intersubband optical absorption in coupled quantum wells under an applied electric field," *Physical Review B*, vol. 38, pp. 8377-8382, 1988.
- [46] P. F. Yuh and K. L. Wang, "Optical transitions in a step quantum well," *Journal of applied physics*, vol. 65, pp. 4377-4381, 1989.
- [47] H. C. Chui, S. M. Lord, E. Martinet, M. M. Fejer, and J. J.S. Harris, "Intersubband transitions in high indium content InGaAs/AlGaAs quantum wells," *Applied Physics Letters*, vol. 63, pp. 364-366, 1993.

## BIOGRAPHICAL INFORMATION

Jeffery Allen received his BSEE from the University of Texas at Arlington in 2001. Jeffery worked for both the defense and commercial industry as an RF and optics engineer. After a short academic break, Jeffery returned to the University of Texas at Arlington to complete his MSEE where he primarily worked in the research areas of theoretical quantum mechanics and infrared photonic devices. Apart from his main thrust in quantum well devices, Jeffery has also conducted research projects in the application of near infrared spectroscopy for noninvasive brain imaging and is published in the field. Jeffery is a member and former officer of the IEEE. He is also affiliated to the Electrical Engineering honor society, Eta Kappa Nu and the Engineering honor society, Tau Beta Pi. After graduation, Jeffery will pursue a career as a Senior Test Engineer at Motorola Networks. Jeffery intends to pursue a PhD in nanophotonics in the years to come.